Spring 4-27-2020

Applications of the Negatively-Charged Silicon Vacancy Color Center in Diamond

Forrest A. Hubert
University of New Mexico

Recommended Citation

Hubert, Forrest A.. "Applications of the Negatively-Charged Silicon Vacancy Color Center in Diamond." (2020). https://digitalrepository.unm.edu/ose_etds/86

Forrest Hubert

Candidate

Optical Science & Engineering

Department

This dissertation is approved, and it is acceptable in quality and form for publication: *Approved by the Dissertation Committee:*

Dr. Victor Acosta, Chair

Dr. Keith Lidke, Member

Dr. Alejandro Manjavacas, Member

Dr. Terefe Habteyes, Member

Applications of the Negatively-Charged Silicon Vacancy Color Center in Diamond

by

Forrest Hubert

B.S., Physics, Brigham Young University - Idaho, 2015

THESIS

Submitted in Partial Fulfillment of the
Requirements for the Degree of

Master of Science
Optical Science & Engineering

The University of New Mexico

Albuquerque, New Mexico

May, 2020

Dedication

For my family.

Acknowledgments

I would first like to thank my thesis advisor, Dr. Victor Acosta of the Physics Department at the University of New Mexico. Prof. Acosta was always available whenever I got stuck or had a question about my research or writing. He consistently allowed this paper to be my own work, but steered me in the right the direction whenever he thought I needed it.

I would also like to thank the members of the quantum nanophotonics and biosensing group at the University of New Mexico, and Dr. Adam S. Backer at Sandia National Labs for their support in proof reading sections of this thesis. I especially would like to thank Yaser Silani, who I worked very closely with on the main experiment.

Finally, I must express my very profound gratitude to my wife, Diane Hubert, for providing me with unfailing support and continuous encouragement throughout my years of study, and through the process of researching, and writing this thesis. This accomplishment would not have been possible without her. Thank you.

Forrest Hubert

Applications of the Negatively-Charged Silicon Vacancy Color Center in Diamond

by

Forrest Hubert

B.S., Physics, Brigham Young University - Idaho, 2015

M.S., Optical Science & Engineering, University of New Mexico, 2020

Abstract

The spatial resolution and fluorescence signal amplitude in stimulated emission depletion (STED) microscopy is limited by the photostability of available fluorophores. Here, we show that negatively-charged silicon vacancy (SiV) centers in diamond are promising fluorophores for STED microscopy, owing to their photostable, near-infrared emission and favorable photophysical properties. A home-built pulsed STED microscope was used to image shallow implanted SiV centers in bulk diamond at room temperature. We performed STED microscopy on isolated SiV centers and observed a lateral full-width-at-half-maximum spot size of 89 ± 2 nm, limited by the low available STED laser pulse energy (0.4 nJ). For a pulse energy of 5 nJ, the resolution is expected to be $\sim$20 nm. We show that the present microscope can resolve SiV centers separated by $\lesssim 150$ nm that cannot be resolved by confocal microscopy. We also review the physical properties of color centers in diamond, and we discuss possible nonlinear optics applications of the SiV color center.

Contents

1 Introduction **1**

1.1 Fluorescence Microscopy 3

1.2 Super Resolution Microscopy 5

2 Theory **7**

2.1 Methods of Measuring Pulse Lengths 7

2.2 Creating a Donut Beam 14

2.3 Polarization Effects of High NA Objectives 20

2.4 Theory Behind SRIM 24

2.5 Franck-Condon Principle 27

2.6 Charge State Instability Near Surfaces 30

2.7 Optical Nonlinearities 35

3 Experiment **39**

3.1 Introduction 39

3.2 Experimental Setup 42

3.3 Results 43

3.4 Discussion and conclusion 47

4 Supplemental Information 49

4.1 Microscope setup 49

4.2 Sample Preparation 51

4.3 Pulse fluence and cross section calculations 51

4.4 Temporal characterization of laser pulses 53

4.5 Lateral PSF in STED microscopy 55

4.6 Fluorescence intensity distribution of isolated SiV centers 58

4.7 Anti-Stokes excitation 59

References 61

Chapter 1

Introduction

A color center is a defect in the crystal lattice that can absorb light in a spectral region where the pure crystal has no absorption. Diamond is a wide-bandgap semiconductor whose valence and conduction band has an energy separation of 5.5 eV. Some defects have optical and spin transitions that fall entirely within the bandgap. These defects are therefore well isolated from the bulk, and can have highly coherent spin and optical properties.

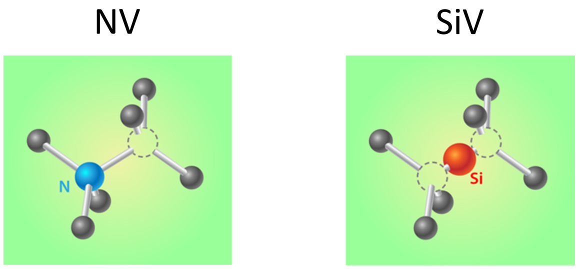

Figure 1.1: The left image is a ball and stick model of a nitrogen vacancy (NV) center. A nitrogen atom replaces a carbon atom in the diamond crystal lattice, and lies nearest-neighbor to a lattice vacancy. The right image is a ball and stick model of a silicon vacancy (SiV) center. A silicon atom replaces two neighboring carbon atoms in the diamond crystal lattice, and is positioned between the two lattice vacancies.

Diamond hosts many color centers because of its wide bandgap. Of the known color centers in diamond, the negatively-charged nitrogen vacancy (NV) color center is probably the most studied defect [1–8]. The NV center is a point defect in the diamond crystal lattice in which a nitrogen atom substitutes for a carbon atom, and lies nearest-neighbor to a lattice vacancy, seen in Figure 1.1. The NV center has been widely studied due to its spin properties including: millisecond coherence times at room temperature, the ability to polarize optically, and the ability to detect spin states by their spin-dependent fluorescence rate. Because of this, the NV center has been studied for applications in quantum information, quantum sensing, and biological imaging. For example, at room temperature two individual NV centers separated by 25 nm, were entangled for 28 μs [9]. The NV center was used to show the violation of the Bell inequality using a loop-hole free measurement [10]. The NV center is used in nuclear magnetic resonance (NMR) spectroscopy, including using microfluidic chips to do NMR spectroscopy on picoliters of liquid analyte [11].

The NV center has also been used in biological imaging, the topic of this thesis. Fluorescent nanodiamonds (FNDs) doped with NV color centers have been functionalized to be used as fluorescent markers to label structures inside cells, excised tissue, or living animals for study [12–16]. FNDs with NV centers have also been used as temperature sensors inside of cells [17]. However, there are downsides to the NV color center which render them sub-optimal for some bio-imaging applications. These include the NV center's broad spectral features (discussed in section 2.5) and its charge state instabilities near surfaces (discussed in section 2.6). The broad spectral features of the NV center cause it to require relatively high optical excitation intensities, which can lead to sample photodamage (chapter 3). The charge state instability near surfaces restricts the minimum size ($\gtrsim$ 10 nm [18, 19]) of FNDs for stable NV centers. This restriction on the minimum size ultimately limits how close the fluorescent label can bind to the target structure. These characteristics of the NV center make it difficult to create a reliable solid-state fluorescent label to compete with other labels used for fluorescent bio-imaging.

Another color center in diamond that has received a lot of attention recently is the negatively-charged silicon vacancy (SiV) color center. The SiV color center is formed by replacing two neighboring carbon atoms in the diamond lattice with one silicon atom, which places itself between the two vacant lattice sites, shown in Figure 1.1. The SiV center charge state has been shown to be stable in nanodiamonds as small as 2 nm in diameter [20], and SiV centers have much narrower spectral features in the near-infrared. These characteristics make SiV centers a promising candidate for use as a fluorescent label in super resolution microscopy.

1.1 Fluorescence Microscopy

Fluorescence microscopy is a contrast-enhancing technique used in numerous fields, including biological imaging. Typically, fluorescent labels are functionalized to bind to structures of interest. These labels provide contrast in samples that do not ordi-

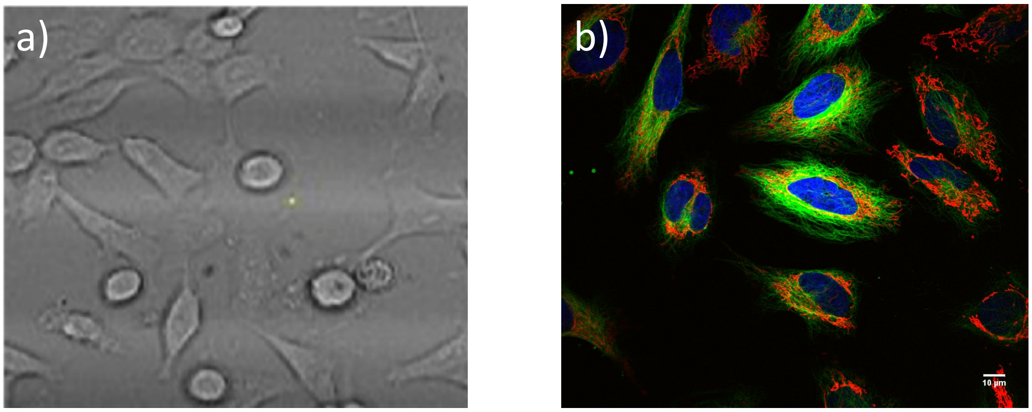

Figure 1.2: (a) Bright field image of HeLa cells. Image adapted from [21]. (b) Multicolor fluorescence image of HeLa cells. Image adapted from [22]. Mitochondria are stained in red (Mitotracker red), the nucleus is stained in blue (DAPI), and the microtubules are stained in green (Tubulintracker green).

narily exhibit fluorescence. Figure 1.2(a) shows a bright-field image of HeLa cells. Bright field images are created by collecting light that has been transmitted through the sample. Contrast is created by the absorption of light in different areas of the sample. Due to the lack of contrast, it is hard to see much else than the outline cell body. Figure 1.2(b) shows a multicolor fluorescent image of HeLa cells. You can distinguish Mitochondria the nucleus is seen in blue, and the microtubules are stained in green. However there are limits to how well the sub-cellular features can be resolved. This is because optical diffraction limits how close two labels can be to one another and still distinguish them apart.

We define the lateral resolution, Δd, in fluorescence microscopy as the full-width at half-maximum (FWHM) of a fluorescence profile created by a point emitter. This lateral resolution is a function of the wavelength of light (λ) and the numerical aperture (NA) of the objective, according to the diffraction limit:

$$\Delta d = \frac{\eta\ \lambda}{2\ \mathrm{NA}}. \tag{1.1}$$

The coefficient η will take different values, and is of order ~ 1, depending on the fluorescence microscopy technique. For example, $\eta \approx 1.22$ in a wide-field epifluorescence microscope and $\eta \approx 1$ in a scanning confocal microscope. For a confocal microscope using red light ($\lambda = 700$ nm), and the highest numerical aperture objectives available ($\mathrm{NA} = 1.4$), the smallest features we can resolve is $\Delta d = 250$ nm. Fortunately, in the past couple decades, techniques have been developed to bypass this fundamental limit and allow us to see features closer than the diffraction limit of light down to ~ 20 nm [23]. These techniques comprise the field of super resolution microscopy.

1.2 Super Resolution Microscopy

Super resolution microscopy is a technique which allows achievable resolutions below the diffraction limit of light. There are two main categories of techniques within far-field super resolution fluorescence microscopy. The first category includes localization based techniques which exploit temporal behaviors of fluorescent labels [24–27]. The second category includes pattern-illumination based techniques that exploit nonlinear responses of fluorescent labels [28, 29]. Some of the scientists that developed the foundations for these techniques were recognized in 2014 with the Nobel Prize in Chemistry, Eric Betzig, Stefan Hell, and W. E. Moerner. The technique discussed in most of this thesis falls under the "Pattern-illumination" category and is called Stimulated Emission Depletion (STED) Microscopy.

To build a foundation to understand STED microscopy, we start by describing scanning confocal microscopy. Confocal microscopy is a fluorescence imaging technique used for optical sectioning, which rejects out of focus light and increases contrast. In Figure 1.3(a) is a diagram showing a scanning confocal microscope. The light source is tightly focused to a diffraction limited spot by the microscope objective, and the sample is scanned. The fluorescence is collected by the objective lens and a pinhole is placed in the collection path to eliminate out of focus light in the fluorescent image. A STED microscope is a modified version of a confocal microscope, where a second donut shaped laser beam is introduced to stimulate emission of the label in a spatially selective manner, shown in Figure 1.3(b). Figure 1.3(c) shows a cartoon illustrating that when the two laser beams are spatially aligned, they alter the point spread function (PSF) of the confocal microscope leading to an improvement in achievable resolution. The lateral resolution for this technique, labeled Δd_{STED}, is:

$$\Delta d_{STED} = \frac{\Delta d_{\mathrm{confocal}}}{\sqrt{1 + I/I_{\mathrm{sat}}}}, \tag{1.2}$$

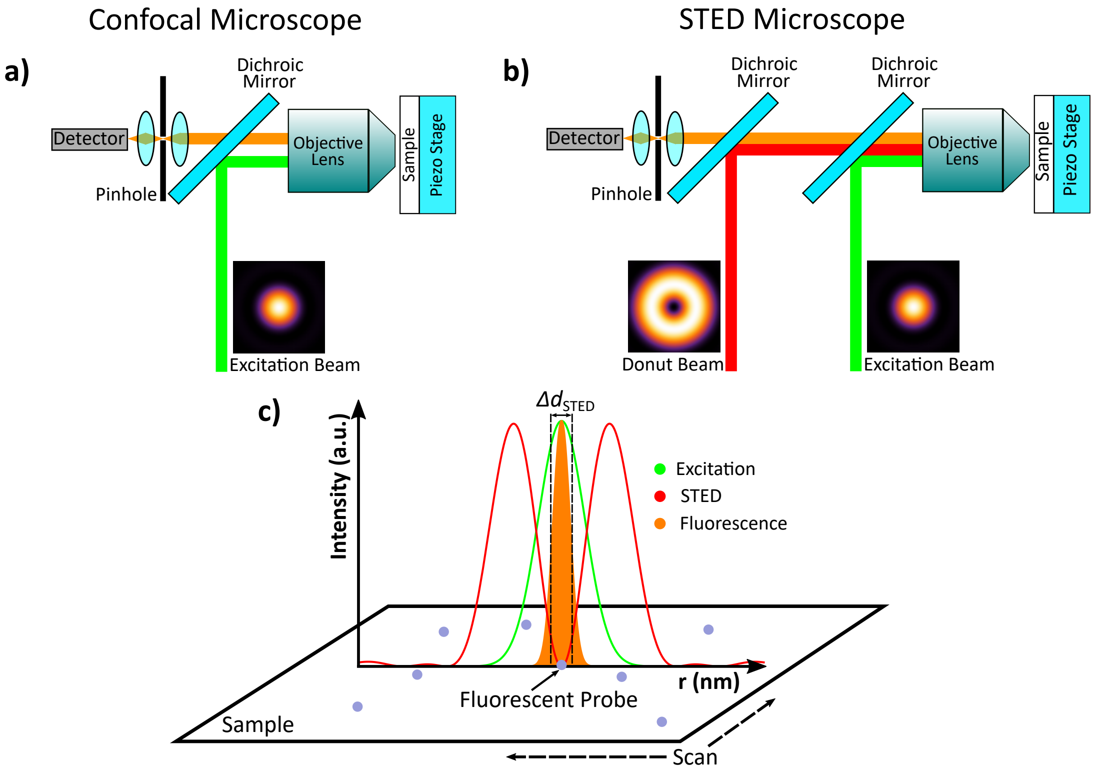

Figure 1.3: (a) Diagram of a confocal microscope. (b) Diagram of a STED microscope. (c) Picture showing how a STED microscope alters the PSF of a confocal microscope. The green intensity distribution is the PSF from a point source in a scanning confocal microscope. When the red intensity distribution, representing the donut beam, is added and the sample is scanned, the PSF gets reduced to the orange intensity distribution which has a resolution smaller than the diffraction limit of a confocal microscope described by equation (1.1).

where Δd is the scanning confocal resolution, I is the intensity of the depletion donut beam, and I_{sat} is the depletion saturation intensity of the fluorescent label. It is worth noting that when $I = 0$, $\Delta d_{\text{STED}} = \Delta d_{\text{confocal}}$.

Chapter 2

Theory

2.1 Methods of Measuring Pulse Lengths

In order to achieve the highest resolutions it is common to use pulses for both excitation and depletion. This allows the microscope to have moderate average intensity to avoid sample photo damage, while achieving high peak intensity for stimulating emission to get the best Δd_{STED}, see equation (1.2). Typically it is desirable to have a pulse duration shorter than the excited state, lifetime so we can stimulate emission before it spontaneously emits. The SiV center excited state lifetime is 1.2 ns [30], so a picosecond pulse duration would be ideal.

For our experiment, we used a supercontinuum laser source to create both the excitation and depletion pulses. We expect the supercontinuum laser source used in these experiments to have a pulse duration of $\tau_p \approx 30$ ps. In order to measure the time trace of an individual pulse, a detector with a bandwidth larger than $1/\tau_p \approx 33$ GHz. Such a detector was not available in our lab.

A common way of measuring the pulse duration for lasers with very short pulses

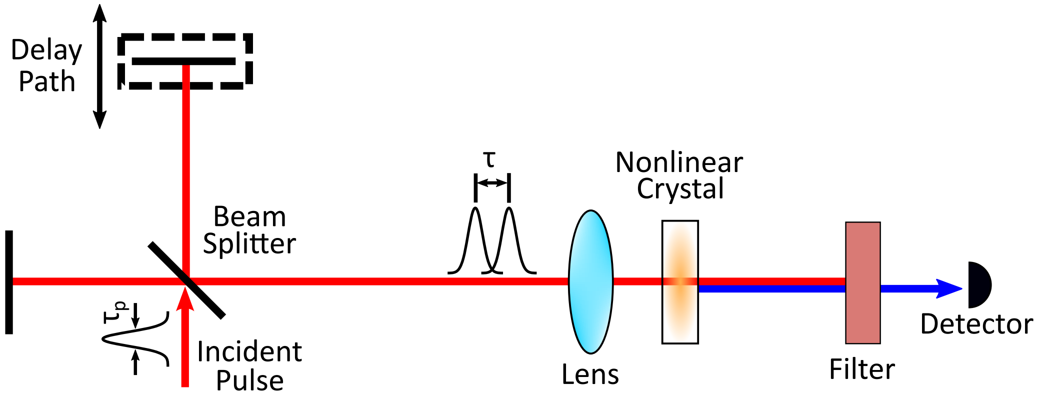

Figure 2.1: Optical diagram of an interferometric autocorrelator. τ is the time delay between the two pulses, and $\tau_p \cdot 2\sqrt{2\ln(2)}$ is the FWHM of the pulse duration.

down in the picosecond and femtosecond ranges is by an optical autocorrelation measurement. The basic principle of this measurement is shown in Figure 2.1. The initial pulse is split into two copies by a beam splitter, which divides the power of the incident pulse equally between the two arms of a Michelson interferometer. The pulse in one of the arms gains a time delay by changing the path length, while the pulse in the other arm has a fixed path length. The pulses are then spatially recombined by the beam splitter and focused into a nonlinear crystal. The two pulses combine, and produce light at twice the optical frequency via a nonlinear process called second harmonic generation (SHG). The initial pulses are filtered and a photodetector records the time-averaged power of the SHG light as a function of the time delay, τ, between the two pulses. Here it no longer matters if the photodetector is too slow to record the waveform of individual pulses because now we are measuring the time-average optical power of the SHG light.

Here we consider a type of autocorrelator called an interferometric autocorrelator, shown in Figure 2.1. The electric field is a function of both space, and time ($E(\vec{r}, t)$). We want to know what happens to $E(\vec{r}, t)$ at the nonlinear crystal, and we define this location as $\vec{r} = 0$. Thus, we only need to evaluate the time dependence. The monochromatic electric field of the incident pulse has the form:

$$E_i(t) = E_0(t)\mathrm{e}^{-i\omega_0 t}. \tag{2.1}$$

The monochromatic electric fields of the two pulse, denoted with subscripts 1 and 2 respectively, can be written as:

$$E_1(t) = \frac{E_0(t)}{\sqrt{2}}\mathrm{e}^{-i\omega_0 t} \qquad\qquad E_2(t) = E_1(t-\tau), \tag{2.2}$$

where $E_0(t)$ is the complex envelope amplitude of the light pulse's electric field, and ω_0 is the angular frequency of the light. When the two pulses spatially recombine on the beam splitter the total field is:

$$E_{\mathrm{tot}}(t,\tau) = E_1(t) + E_2(t). \tag{2.3}$$

The detector integrates over the envelope of a single SHG pulse created at the nonlinear crystal. The detected SHG signal, $A(\tau)$, is proportional to the time average of the square of the incident optical intensity. The proportionality constant, ϵ, depends on the efficiency to create SHG in the nonlinear crystal. The response time of the detector is much slower than the pulse duration. In this approximation, we can effectively assume that the SHG signal is proportional to the time integral of $|E_{\mathrm{tot}}^2(t,\tau)|^2$ from $-\infty$ to ∞ with respect to a single pulse. In this case, we can express $A(\tau)$ as:

$$\begin{aligned}
\frac{A(\tau)}{\epsilon} &= \int_{-\infty}^{\infty} \left|E_{\text{tot}}^2(t,\tau)\right|^2 dt \\
&= \int_{-\infty}^{\infty} \left|[E_1(t)+E_2(t)]^2\right|^2 dt \\
&= \int_{-\infty}^{\infty} \left|E_1^2(t)+2E_1(t)E_1(t-\tau)+E_1^2(t-\tau)\right|^2 dt \\
&= \int_{-\infty}^{\infty} E_1^2(t)E_1^{*2}(t)dt \\
&+ \int_{-\infty}^{\infty} E_1^2(t-\tau)E_1^{*2}(t-\tau)dt \\
&+ 2\int_{-\infty}^{\infty} E_1^2(t)E_1^{*}(t)E_1^{*}(t-\tau)dt \\
&+ \int_{-\infty}^{\infty} E_1^2(t)E_1^{*2}(t-\tau)dt \\
&+ 2\int_{-\infty}^{\infty} E_1(t)E_1(t-\tau)E_1^{*2}(t)dt \\
&+ 4\int_{-\infty}^{\infty} E_1(t)E_1(t-\tau)E_1^{*}(t)E_1^{*}(t-\tau)dt \\
&+ 2\int_{-\infty}^{\infty} E_1(t)E_1(t-\tau)E_1^{*2}(t-\tau)dt \\
&+ \int_{-\infty}^{\infty} E_1^2(t-\tau)E_1^{*2}(t)dt \\
&+ 2\int_{-\infty}^{\infty} E_1^2(t-\tau)E_1^{*}(t)E_1^{*}(t-\tau)dt. \qquad (2.4)
\end{aligned}$$

The first two terms in equation (2.4) are known as the background intensity, A_{back}:

$$\begin{aligned}
\frac{A_{\text{back}}}{\epsilon} &= \int_{-\infty}^{\infty} E_1^2(t)E_1^{*2}(t)dt \\
&+ \int_{-\infty}^{\infty} E_1^2(t-\tau)E_1^{*2}(t-\tau)dt \\
&= \int_{-\infty}^{\infty} \left[\left|\frac{E_0(t)}{\sqrt{2}}\right|^4 + \left|\frac{E_0(t-\tau)}{\sqrt{2}}\right|^4\right] dt \\
&= \frac{1}{2}\int_{-\infty}^{\infty} I^2(t)dt. \qquad (2.5)
\end{aligned}$$

Here $I(t) = |E_0(t)|^2$ and is proportional to the incident intensity when $\tau = 0$. The 6th term in equation (2.4) is known as the intensity autocorrelation, $A_{\text{int}}(\tau)$:

$$\begin{aligned}
\frac{A_{\text{int}}(\tau)}{\epsilon} &= 4\int_{-\infty}^{\infty} E_1(t)E_1(t-\tau)E_1^*(t)E_1^*(t-\tau)dt \\
&= 4\int_{-\infty}^{\infty} \left|\frac{E_0(t)}{\sqrt{2}}\right|^2 \left|\frac{E_0(t-\tau)}{\sqrt{2}}\right|^2 dt \\
&= \int_{-\infty}^{\infty} I(t)I(t-\tau)dt. \qquad (2.6)
\end{aligned}$$

Terms 3, 5, 7, and 9 in equation (2.4) are the coherence terms oscillating at optical frequency ω_0, $A_{\omega_0}(\tau)$:

$$\begin{aligned}
\frac{A_{\omega_0}(\tau)}{\epsilon} &= 2\int_{-\infty}^{\infty} E_1^2(t)E_1^*(t)E_1^*(t-\tau)dt \\
&+ 2\int_{-\infty}^{\infty} E_1(t)E_1(t-\tau)E_1^{*2}(t)dt \\
&+ 2\int_{-\infty}^{\infty} E_1(t)E_1(t-\tau)E_1^{*2}(t-\tau)dt \\
&+ 2\int_{-\infty}^{\infty} E_1^2(t-\tau)E_1^*(t)E_1^*(t-\tau)dt \\
&= 2\int_{-\infty}^{\infty} \left|\frac{E_0(t)}{\sqrt{2}}\right|^2 \text{Re}\left[\frac{E_0(t)}{\sqrt{2}}\frac{E_0^*(t-\tau)}{\sqrt{2}}\text{e}^{-i\omega_0\tau}\right] dt \\
&+ 2\int_{-\infty}^{\infty} \left|\frac{E_0(t)}{\sqrt{2}}\right|^2 \text{Re}\left[\frac{E_0(t)}{\sqrt{2}}\frac{E_0^*(t-\tau)}{\sqrt{2}}\text{e}^{-i\omega_0\tau}\right] dt \\
&+ 2\int_{-\infty}^{\infty} \left|\frac{E_0(t-\tau)}{\sqrt{2}}\right|^2 \text{Re}\left[\frac{E_0(t)}{\sqrt{2}}\frac{E_0^*(t-\tau)}{\sqrt{2}}\text{e}^{-i\omega_0\tau}\right] dt \\
&+ 2\int_{-\infty}^{\infty} \left|\frac{E_0(t-\tau)}{\sqrt{2}}\right|^2 \text{Re}\left[\frac{E_0(t)}{\sqrt{2}}\frac{E_0^*(t-\tau)}{\sqrt{2}}\text{e}^{-i\omega_0\tau}\right] dt \\
&= \int_{-\infty}^{\infty} I(t)\text{Re}\left[E_0(t)E_0^*(t-\tau)\text{e}^{-i\omega_0\tau}\right] dt \\
&+ \int_{-\infty}^{\infty} I(t-\tau)\text{Re}\left[E_0(t)E_0^*(t-\tau)\text{e}^{-i\omega_0\tau}\right] dt \\
&= \int_{-\infty}^{\infty} \left(I(t) + I(t-\tau)\right)\text{Re}\left[E_0(t)E_0^*(t-\tau)\text{e}^{-i\omega_0\tau}\right] dt. \qquad (2.7)
\end{aligned}$$

Terms 4, and 8 in equation (2.4) are the coherence terms oscillating at angular frequency $2\omega_0$, $A_{2\omega_0}(\tau)$:

$$\begin{aligned}\frac{A_{2\omega_0}(\tau)}{\epsilon} &= \int_{-\infty}^{\infty} E_1^2(t)E_1^{*2}(t-\tau)dt \\ &+ \int_{-\infty}^{\infty} E_1^2(t-\tau)E_1^{*2}(t)dt \\ &= 2\int_{-\infty}^{\infty} \mathrm{Re}\left[\left(\frac{E_0(t)}{\sqrt{2}}\right)^2\left(\frac{E_0^*(t-\tau)}{\sqrt{2}}\right)^2 \mathrm{e}^{-i2\omega_0\tau}\right]dt \\ &= \frac{1}{2}\int_{-\infty}^{\infty} \mathrm{Re}\left[E_0^2(t)E_0^{*2}(t-\tau)\mathrm{e}^{-i2\omega_0\tau}\right]dt. \end{aligned} \tag{2.8}$$

Therefore the interferometric autocorrelation intensity detected has the following terms:

$$A(\tau) = A_{\text{back}} + A_{\text{int}}(\tau) + A_{\omega_0}(\tau) + A_{2\omega_0}(\tau). \tag{2.9}$$

It is common to normalize this to the background A_{back}:

$$A(\tau) = 1 + \frac{A_{\text{int}}(\tau)}{A_{\text{back}}} + \frac{A_{\omega_0}(\tau)}{A_{\text{back}}} + \frac{A_{2\omega_0}(\tau)}{A_{\text{back}}}. \tag{2.10}$$

The maximum signal happens when the recombination of the two pulses undergoes perfect constructive interference at $\tau = 0$, The SHG signal takes the form:

$$\begin{aligned} A(0) &= A_{\text{back}} + A_{\text{int}}(0) + A_{\omega_0}(0) + A_{2\omega_0}(0) \\ &= 8A_{\text{back}}. \end{aligned} \tag{2.11}$$

The background signal happens when $\tau \gg \tau_p$, in this case the SHG signal takes the form:

$$A(\tau \gg \tau_p) = A_{\text{back}}, \tag{2.12}$$

where the other 3 terms in equation (2.9) go to zero because there is no overlap between the pulses nor interference.

In order to measure the pulse duration from the SHG signal produced by the autocorrelator, you must assume a pulse shape for the incident pule. For example,

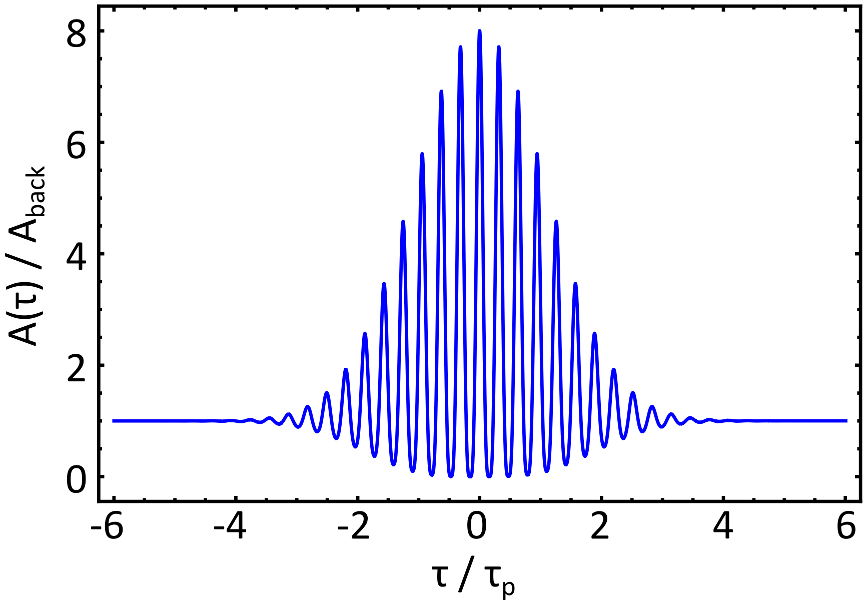

Figure 2.2: SHG signal, $A(\tau)/A_{\text{back}}$, as a function of the normalized time delay, τ/τ_p. Calculated from equation (2.14) using $\omega_0 = 20$ THz and $\tau_p = 1$ ps.

for a Gaussian shaped incident pulse,

$$E_0(t) = \mathrm{e}^{-\frac{1}{2}\left(\frac{t}{\tau_p}\right)^2}, \tag{2.13}$$

equation (2.10) then takes takes the form:

$$\frac{A(\tau)}{A_{\text{back}}} = 1 + [2 + \cos(2\omega_0\tau)]\ \mathrm{e}^{-\frac{1}{2}\left(\frac{\tau}{\tau_p}\right)^2} + 4\ \cos(\omega_0\tau)\ \mathrm{e}^{-\frac{3}{8}\left(\frac{\tau}{\tau_p}\right)^2}. \tag{2.14}$$

Figure 2.2 shows an example of a complete interferometric autocorrelation signal according to equation (2.14). The shape of the upper envelope of equation (2.14) has the form [31]:

$$\left.\frac{A(\tau)}{A_{\text{back}}}\right|_{\omega_0\tau=0} = 1 + 3\ \mathrm{e}^{-\frac{1}{2}\left(\frac{\tau}{\tau_p}\right)^2} + 4\ \mathrm{e}^{-\frac{3}{8}\left(\frac{\tau}{\tau_p}\right)^2}, \tag{2.15}$$

and the lower envelope of equation (2.14) has the form [31]:

$$\left.\frac{A(\tau)}{A_{\text{back}}}\right|_{\omega_0\tau=\pi} = 1 + 3\ \mathrm{e}^{-\frac{1}{2}\left(\frac{\tau}{\tau_p}\right)^2} - 4\ \mathrm{e}^{-\frac{3}{8}\left(\frac{\tau}{\tau_p}\right)^2}. \tag{2.16}$$

You can fit for the pulse duration using equation (2.15) or (2.16), assuming a Gaussian incident pulse.

There are other types of autocorrelators other than the one shown in Figure 2.1. For example, one type uses a photodiode with a large bandgap semi-conductor material as both the nonlinear crystal, and the detector. This method requires that only two-photon absorption in the photodiode can create a photo-electron, whereas one photon absorption does not create a large photo current. Silicon photodetectors have one-photon absorption in the range 400 nm to 1000 nm, which makes it possible to characterize pulses in the wavelength range approximately 1050 nm to 2 μm. In the near-infrared (NIR), 700 nm to 1000 nm, it is tempting to think one can use a Gallium Phosphide (GaP) photodetector, which has one-photon absorption in the range 150 nm to 550 nm. However, the quantum efficiency for two-photon absorption in the NIR was low for these detectors.

We attempted to do a measurement similar to Figure 2.1 with a Potassium Dihydrogen Phosphate (KDP) nonlinear crystal. However, the peak pulse intensities available in our laser were not high enough to create efficient SHG signals. We ended up using the SiV color center nonlinear optical properties to determine the pulse duration. The methods we used are discussed in section 4.4.

2.2 Creating a Donut Beam

In order to understand how a donut beam intensity distribution is created, we will first describe the intensity distribution of a more simple system, a circular aperture. From there we can show how to modulate the resulting intensity distribution to form a donut.

First, we need to build the ground work for diffraction in the far-field. This can be described by the Fresnel-Huygens diffraction integral [32,33]:

$$E(x,y) = \frac{i}{\lambda}\int_{\Sigma} E(\xi,\eta)\frac{\mathrm{e}^{ikr}}{r}cos\theta\ d\Sigma. \tag{2.17}$$

Equation (2.17) describes the complex electric field in the image plane, $E(x,y)$, that results from a complex electric field in the Fourier plane, $E(\xi,\eta)$, separated by a distance z. The Fresnel-Huygens diffraction integral describes the geometry of Figure 2.3, where r is the distance between points $P_1(\xi,\eta)$, and $P(x,y)$, and Σ is the cross sectional area of the beam. According to the Fresnel-Huygens principle, every point of $E(\xi,\eta)$ can be viewed as a point source. The final field $E(x,y)$ is the sum of all the contributions of those point sources, including possible interference. We can convert this to Cartesian coordinates by:

$$\begin{aligned} r &= z\sqrt{1+\left(\frac{\xi-x}{z}\right)^2+\left(\frac{\eta-y}{z}\right)^2} \\ &\approx z\left[1+\frac{1}{2}\left(\frac{\xi-x}{z}\right)^2+\frac{1}{2}\left(\frac{\eta-y}{z}\right)^2\right]. \end{aligned}$$

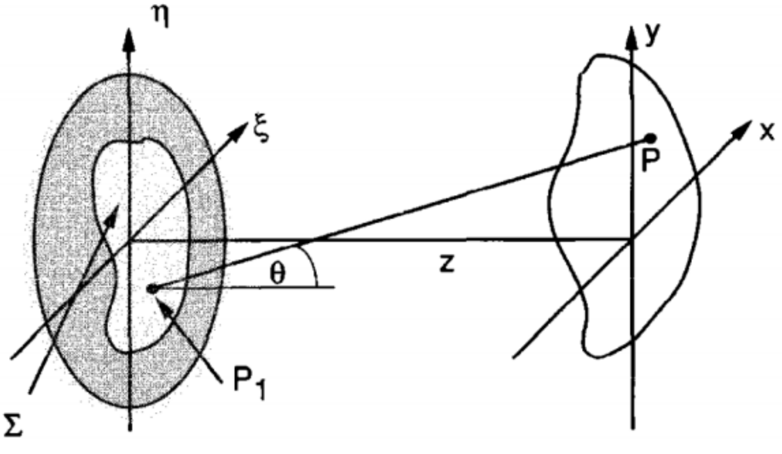

Figure 2.3: Diffraction geometry described by equation (2.17), the variables are described in the text. Image from Goodman, Introduction to Fourier Optics 3ed, 2005 [32].

Where we did a binomial expansion because $z \gg \xi - x$ and $z \gg \eta - y$. We can also include the finite size of the beam. This allows us to re-write equation (2.17) in Cartesian coordinates:

$$E(x,y) = \frac{i\mathrm{e}^{ikz}}{\lambda z}\mathrm{e}^{\frac{ik}{2z}(x^2+y^2)}\iint_{-\infty}^{\infty} E(\xi,\eta)\mathrm{e}^{\frac{ik}{2z}(\xi^2+\eta^2)}\mathrm{e}^{-\frac{ik}{z}(\xi x+\eta y)}d\xi d\eta. \tag{2.18}$$

We can simplify equation (2.18) further under the far-field approximation $z \gg \frac{k(\xi^2+\eta^2)}{2}$:

$$E(x,y) = \frac{i\mathrm{e}^{ikz}}{\lambda z}\mathrm{e}^{\frac{ik}{2z}(x^2+y^2)}\iint_{-\infty}^{\infty} E(\xi,\eta)\mathrm{e}^{-\frac{ik}{z}(\xi x+\eta y)}d\xi d\eta. \tag{2.19}$$

Equation (2.19) is known as the Fraunhofer integral, and is only valid in the far-field when z is very large.

Figure 2.4 shows an aperture with circular geometry. We can calculate the electric field distribution at a distance D from the aperture by converting equation (2.19) to cylindrical coordinates, where (ρ, Φ) are the coordinates at the plane of the aperture, and (q, ϕ) are the coordinates at the plane D away from the aperture. It can be shown

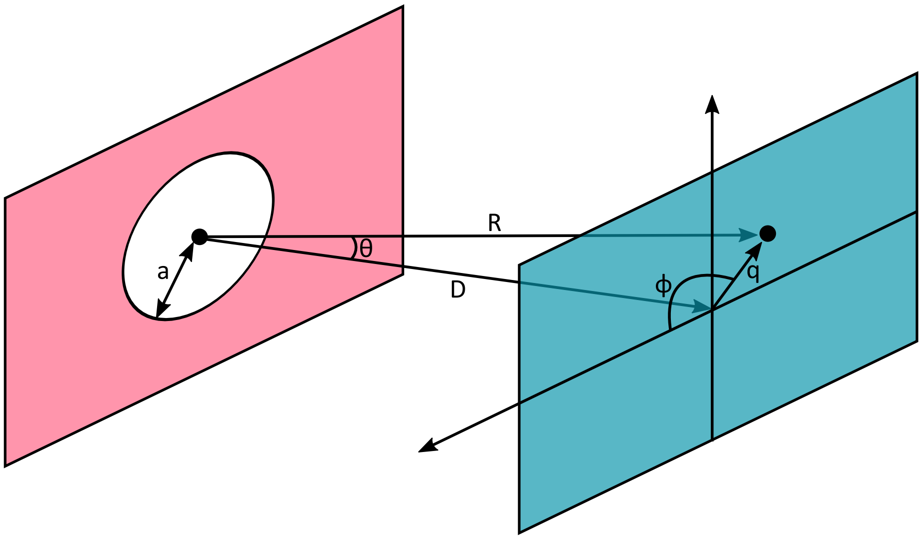

Figure 2.4: Diffraction at a circular aperture. Light is incident from the left of the aperture which has a radius a, and is a distance D from the image plane.

that equation (2.19) then becomes [34]:

$$E(q,\phi) \propto \frac{1}{D}\int_{\rho=0}^{a}\int_{\Phi=0}^{2\pi} E(\rho,\Phi)\mathrm{e}^{i(k\rho q/D)\cos(\phi-\Phi)}\rho d\rho d\Phi. \tag{2.20}$$

If the incident field on the aperture is a plane wave, then the electric field at the aperture is independent of ρ and Φ. We can set $E(\rho,\Phi) = 1$. From the rotational symmetry in the problem, we can take $\phi = 0$, this integral is then:

$$\int_{\rho=0}^{a}\int_{\Phi=0}^{2\pi} \mathrm{e}^{i(k\rho q/D)\cos(\Phi)}\rho d\rho d\Phi. \tag{2.21}$$

The inner integral has the form of $J_0(u)$, which is the zero-th order Bessel function of the first kind, where $u = k\rho q/D$,

$$J_0(u) = \frac{1}{2\pi}\int_0^{2\pi} \mathrm{e}^{u\ \cos\ \nu} d\nu. \tag{2.22}$$

We can use an identity of $J_0(u)$:

$$\int_0^{w} J_0(u)udu = wJ_1(w). \tag{2.23}$$

These two allow us to rewrite equation (2.21) as:

$$E(q) \propto \frac{2\pi D}{(kq)^2}\int_{u=0}^{u=kaq/D} J_0(u)udu = 2\frac{\pi a^2}{D}\frac{J_1(kaq/D)}{kaq/D}. \tag{2.24}$$

If we place a lens with focal length $f = D$ at the position of the circular aperture, it can be shown that we get an intensity distribution $I(q)$:

$$I(q) = I_0\left[2\frac{J_1(kaq/f)}{(kaq/f)}\right]^2. \tag{2.25}$$

This intensity distribution is known as the Airy function with a center intensity I_0. The intensity distribution from equation (2.25) is a common result from fluorescence of a point source through a microscope. In microscopy, it is useful to express $I(q)$ in terms of experimental constants like the wavelength of light (λ), and the numerical aperture (NA) of the objective. When we replace (kaq/f) with those experimental constants, we get:

$$I(q) = I_0\left[2\frac{J_1(\frac{2\pi q\mathrm{NA}}{\lambda})}{(\frac{2\pi q\mathrm{NA}}{\lambda})}\right]^2. \tag{2.26}$$

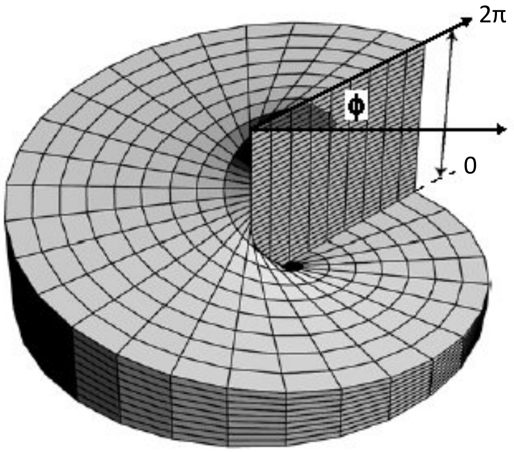

Figure 2.5: Phase distribution of the beam described by (2.27). Image from Leach *et al.* (2004) [35].

Now that we have derived the intensity distribution for an Airy pattern, we can derive the intensity distribution for a donut beam. This is rather simple now that we have the ground work done. We start with equation (2.20), and rather than make the assumption that $E(\rho, \Phi) = 1$, we assume it has a phase that linearly changes with Φ from $0 - 2\pi$ while still being a plane wave, and independent of ρ. This type of phase distribution is known as a vortex phase with a topological charge of 1:

$$E(\Phi) = \mathrm{e}^{i\Phi}. \tag{2.27}$$

Figure 2.5 shows a three-dimensional representation of this phase distribution [35]. Please note that at the center of the beam, all phases of light are present which cause destructive interference. This ideally creates a null intensity spot at the center, which is why this type of beam is called a donut beam. For this phase distribution in cylindrical coordinates, equation (2.20) then becomes:

$$E(q, \phi) \propto \frac{1}{D} \int_{\rho=0}^{a} \int_{\Phi=0}^{2\pi} \mathrm{e}^{i(\Phi + k\rho q/D)\cos(\Phi)} \rho d\rho d\Phi. \tag{2.28}$$

Now in this case, the inner integral has the form of the first-order Bessel function of the first kind, where $u = k\rho q/D$:

$$J_1(u) = \frac{1}{2\pi i}\int_0^{2\pi} \mathrm{e}^{i(\nu+u\ \cos\ \nu)}d\nu. \tag{2.29}$$

Here we can use the approximation [36]:

$$\int_0^u J_1(w)wdw = \frac{\pi}{2}u[J_1(u)H_0(u) - J_0(u)H_1(u)], \tag{2.30}$$

where H_0 and H_1 are known as the zeroth-order and first-order Struve functions, respectively. Place a lens at the aperture, and use the experimental constants (λ, and NA), we get an intensity distribution for the donut shaped beam:

$$I(q) = I_0\left[\pi\frac{J_1(\frac{2\pi q\mathrm{NA}}{\lambda})H_0(\frac{2\pi q\mathrm{NA}}{\lambda}) - J_0(\frac{2\pi q\mathrm{NA}}{\lambda})H_1(\frac{2\pi q\mathrm{NA}}{\lambda})}{(\frac{2\pi q\mathrm{NA}}{\lambda})}\right]^2. \tag{2.31}$$

A graph of both equation (2.26), and (2.31) is shown in Figure 2.6 for the same I_0. This Figure shows us that we get the null intensity at the centre of the donut beam. Notice that the peak intensities are different due to energy conservation.

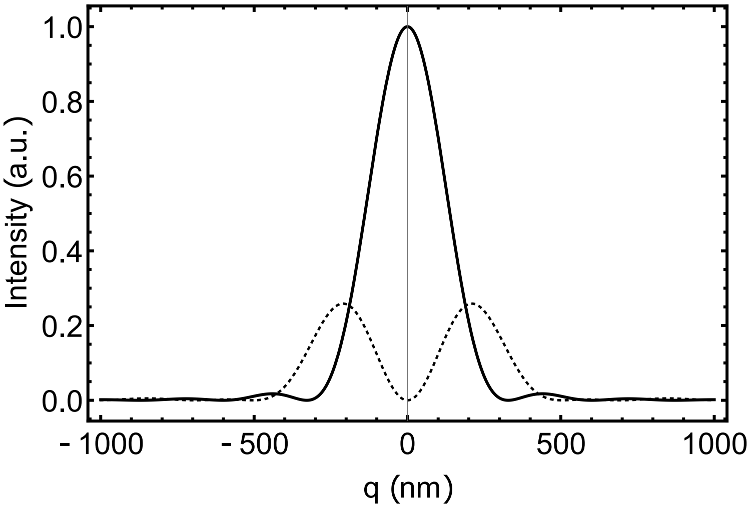

Figure 2.6: Intensity profiles for both an Airy function (solid) and a donut beam (dotted).

Experimentally this phase distribution is generally made by using a vortex phase plate (VPP). These phase plates can create nearly perfect vortex phases, but each element works for only specific wavelengths. The VPP generates the required phase to create the donut shaped beam profile necessary for STED microscopy.

2.3 Polarization Effects of High NA Objectives

In section 2.2, equation (2.17) assumes that all parts of the beam interfere freely, neglecting polarization. This is not necessarily the case in experiment. The analysis in the previous section holds up well if the light is linearly polarized. However, focusing optics with high NA have been shown to produce depolarization effects [38]. These depolarization effects may have an impact on the shape of the donut when focused.

Figure 2.7 shows how two objective lenses with different NA effect the shape of

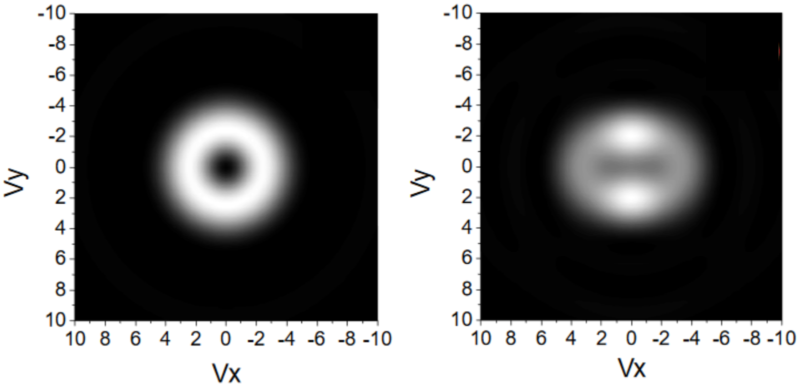

Figure 2.7: Calculated intensity distributions of the focal region of a donut, with linear polarization along the x-direction, focused with an objective NA = 0.2 (left), and NA = 1.0 (right). $V_{x,y}$ are defined as transverse optical coordinates where $V_{x,y} = k[x,y]\sin(\alpha)$, where k is the wave number and α is the maximum angle of convergence. Image from Ganic *et al.* (2003) [37].

the same donut beam polarized along the x-direction [37]. The left image, focused with an objective NA = 0.2, agrees well with the intensity profile we got in Section 2.2. The right image, focused with an objective NA = 1, shows that the same donut beam will distort due to the higher NA objective. The donut rotational symmetry has disappeared, along with the null intensity at the center.

To understand why the donut profile is distorted, we can look at each of its electric field components. Figure 2.8 shows all the components of the electric field of the donut beam in Figure 2.7(b). Figure 2.8(a) shows that the distortion of the donut shape comes from the objective lens bending the electric field along the polarization

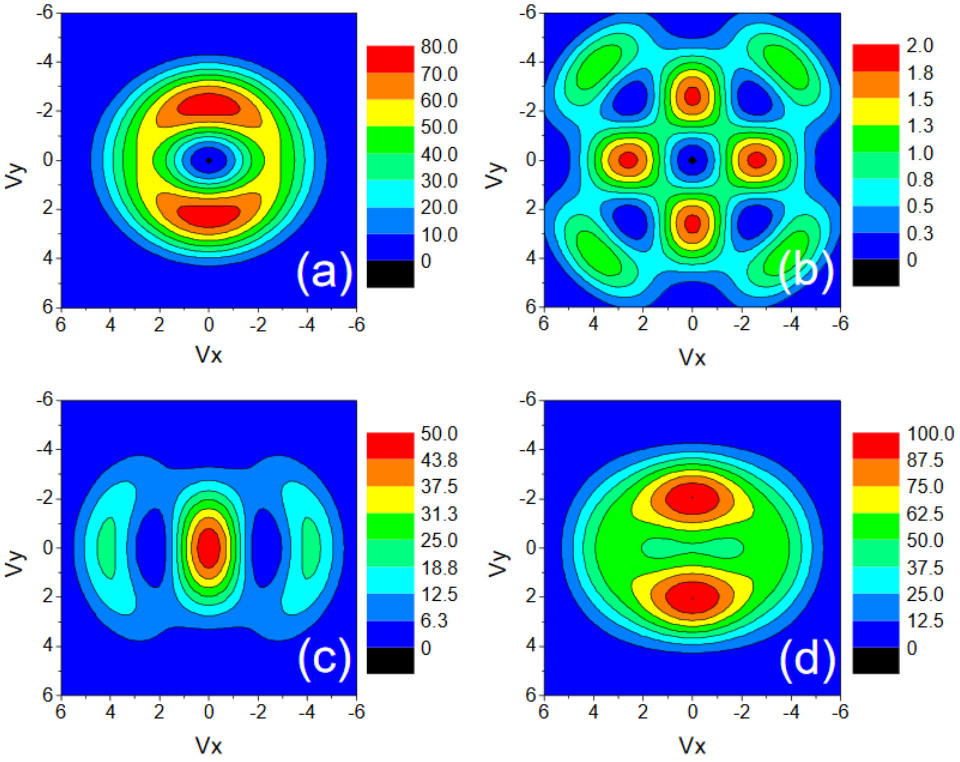

Figure 2.8: Intensity distributions of a donut beam in the focal plane of an objective with NA = 1 for each component of the electric field, E_{total}. (a) $|E_x|^2$, (b) $|E_y|^2$, (c) $|E_z|^2$, (d) $|E_{\text{total}}|^2$. Polarization incident to the objective lens is along the x-direction. Image from Ganic *et al.* (2003) [37].

direction. Figure 2.8(c) shows that the objective lens introduces a relatively large axial component of the electric field (E_z). E_z concentrates nearly all its intensity in the center, causing the overall null intensity of the donut to disappear. The intensity at the center of the focal region for the distorted donut is 49% of the peak intensity, seen in Figure 2.8(d) [37].

The strength of E_z was observed to increase with the NA of the objective lens used to focus the donut beam [37]. Figure 2.9 shows the dependence of $|E_z|^2/|E_x|^2$ on the NA of the objective lens for different values of topological charge, we are only interested in charge 1 (solid black line) as discussed in section 2.2. From the figure we can see the peak intensity ratio is relatively small for NA < 0.3, but increases quickly past the NA $= 0.4$ mark. The dependence shown in Figure 2.9 shows that the polarization of the donut beam has a large impact on the intensity of the focus when using high NA objectives.

The distortion of a donut beam in high NA objective lenses can be minimized by using circular polarization [39]. Figure 2.10 shows two intensity profiles of a donut

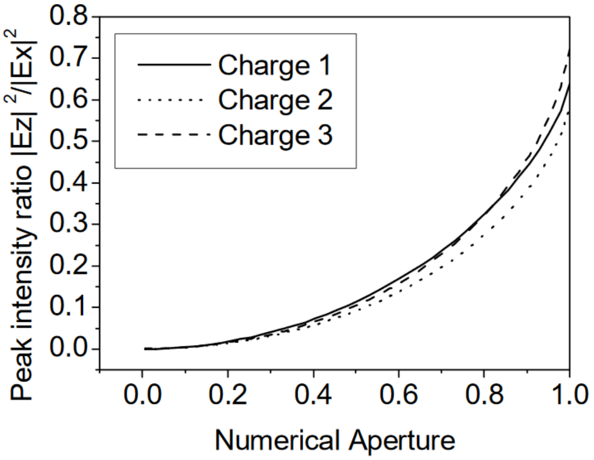

Figure 2.9: The ratio of $|E_z|^2 / |E_x|^2$ as a function of the NA of an objective lens for different topological charges of donut beams. Image from Ganic *et al.* (2003) [37].

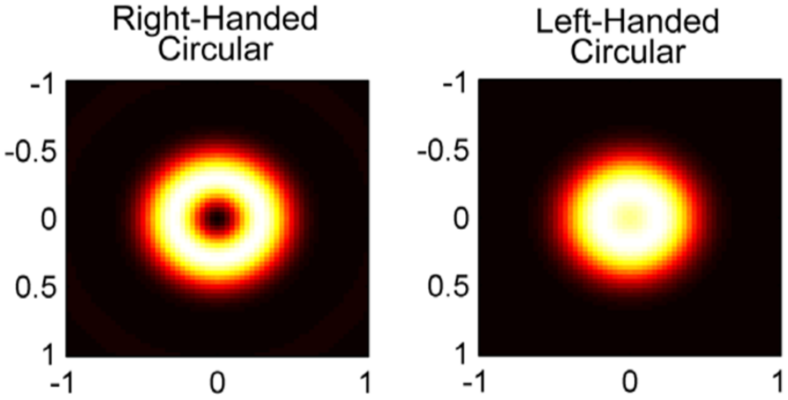

Figure 2.10: Calculated intensity distributions of the focal region of a donut focused with an objective NA = 1.4. The left image shows right-handed circular (RHC) polarization. The right image shows left-handed circular (LHC) polarization. Note that the vortex phase is in the same direction as the right-handed circular polarization. The axis units are in wavelengths. Image from Hao *et al.* (2010) [39]

beam in the focal plane of an objective with NA = 1.4. If circular polarization is used in the same direction as the vortex phase of the electric field, than we get an intensity profile that matches well with our calculations in section 2.2. This is because under circular polarization the phase of E_z will be modulated such that different rays will cancel out their intensities at the focal point. Conversely, if the circular polarization is in the opposite direction of the vortex phase, than the resulting donut has a higher portion of its intensity in the center. Figure 2.10(b) shows a higher intensity in the center of the donut beam than for the linearly polarized case from Figure 2.7(b), albeit keeping its angular symmetry.

Polarization plays a big role in the quality of the donut beam achievable using high NA objective lenses. STED microscopy requires using high NA objective lenses because they increase the resolution achievable. In order to achieve the highest possible resolution in STED microscopy, it is important to understand the role polarization plays in the experiment.

2.4 Theory Behind SRIM

The diamond samples we used in experiments were implanted with silicon ions at 100 keV. This energy controls the distribution depth into the material that the ions will end up. In order to understand the range of depths of ions implanted into the diamond samples, we need to calculate the stopping power of the ion, $^{28}\mathrm{Si}^{+}$, in the material being implanted, diamond. The stopping power of a material is defined by the loss of energy, E, per unit path length, x:

$$S(E) = -\frac{dE}{dx}. \tag{2.32}$$

The stopping power has two main components, the electronic and the nuclear stopping power. The electronic stopping power results from inelastic collisions between the ion with the bound electrons in the medium. The nuclear stopping power comes from elastic collisions between the ion and the atoms in the medium. The Bethe formula is commonly used to describe the expectation value of the electronic

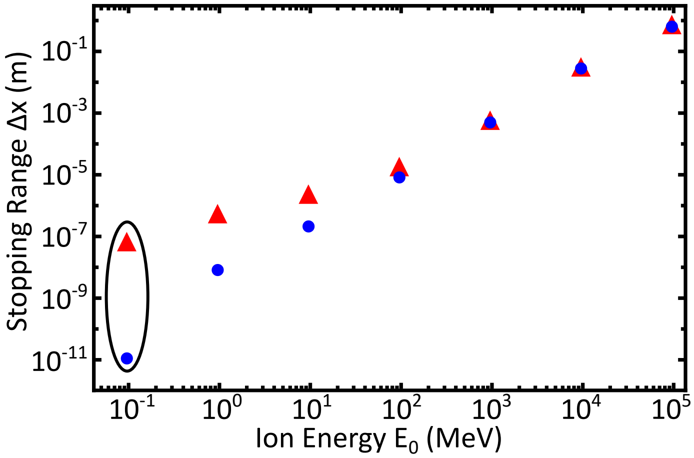

Figure 2.11: Stopping range, Δx, as a function of the ion energy, E_0, for $^{28}\mathrm{Si}^{+}$ in diamond. The blue circles are calculated using equation (2.34), $n = 1.06 \times 10^{24}$ cm^{-3}, and $I = 90$ eV were used. The red triangles are calculated using the SRIM software. The two data points circled in black are the stopping range for the energy used to create the samples for our experiment, 100 keV.

stopping power in a continuous material:

$$-\left\langle \frac{dE}{dx} \right\rangle = \frac{4\pi}{m_e c^2} \cdot \frac{nz^2}{\beta^2} \cdot \left(\frac{e^2}{4\pi\epsilon_0} \right)^2 \cdot \left[\ln \left(\frac{2m_e c^2 \beta^2}{I \cdot (1 - \beta^2)} \right) - \beta^2 \right], \tag{2.33}$$

where m_e is the rest mass of an electron, c is the speed of light, z is the total number of electrons of the ion, $\beta = v/c$, v is the speed of the ion, n is the electron number density of the material, e is the charge of an electron, ϵ_0 is the vacuum permitivity, and I is the mean excitation potential of the material. The mean stopping range, Δx, can then be calculated from the stopping power:

$$\Delta x = \int_0^{E_0} \frac{1}{\langle S(E) \rangle} dE, \tag{2.34}$$

where E_0 is the initial kinetic energy of the ion.

The blue circles in Figure 2.11 show values of Δx as a function of E_0 using the Bethe equation for $^{28}\text{Si}^+$ implanted into diamond. For silicon at high energies ($\gtrsim$ 100 MeV), the electronic stopping power is the dominant term and the nuclear stopping power can be neglected. However, at lower energies the nuclear stopping power plays a significant role. Also to note is that equation (2.33) is an expectation value, not a distribution. In reality, diamond is a crystal lattice and energy loss happens in discrete quantities and at discrete locations. In order to get the distribution of ion locations you would have to use a Monte-Carlo method to keep track of the stopping locations of many ions. A software suite that is widely used for this purpose is called "The Stopping and Range of Ions in Matter", or SRIM. The red triangles in Figure 2.11 are values of Δx for $^{28}\text{Si}^+$ in diamond calculated by SRIM. The blue circles differ from the red triangles significantly at energies $<$ 100 MeV where the nuclear stopping power is non-negligible.

SRIM uses a quantum mechanical treatment of ion-atom collisions to calculate the stopping, and range of ions into matter [40]. The simulation performs a Monte-Carlo method for a user chosen number of ions, and calculates the stopping range for each ion in order to get an experimentally accurate range. This software takes into account many corrections to equation (2.33), such as: shell corrections, mean ionization potentials, the effective charge of ions, the Fermi velocity of solids, etc. It also takes into account the nuclear stopping power using their own semi-empirical formula. Figure 2.12 shows the simulated distribution of ion ranges of ^{28}Si^{+} at 100 keV in diamond. During implantation, each ion creates a number of lattice vacancies in its wake. After implantation, the samples are then annealed for 4 hours at 800C and 2 hours at 1100C in a vacuum furnace. During this process, the vacancies are mobile whereas the silicon atoms are not. The final distribution of SiV centers resembles the distribution shown in Figure 2.12.

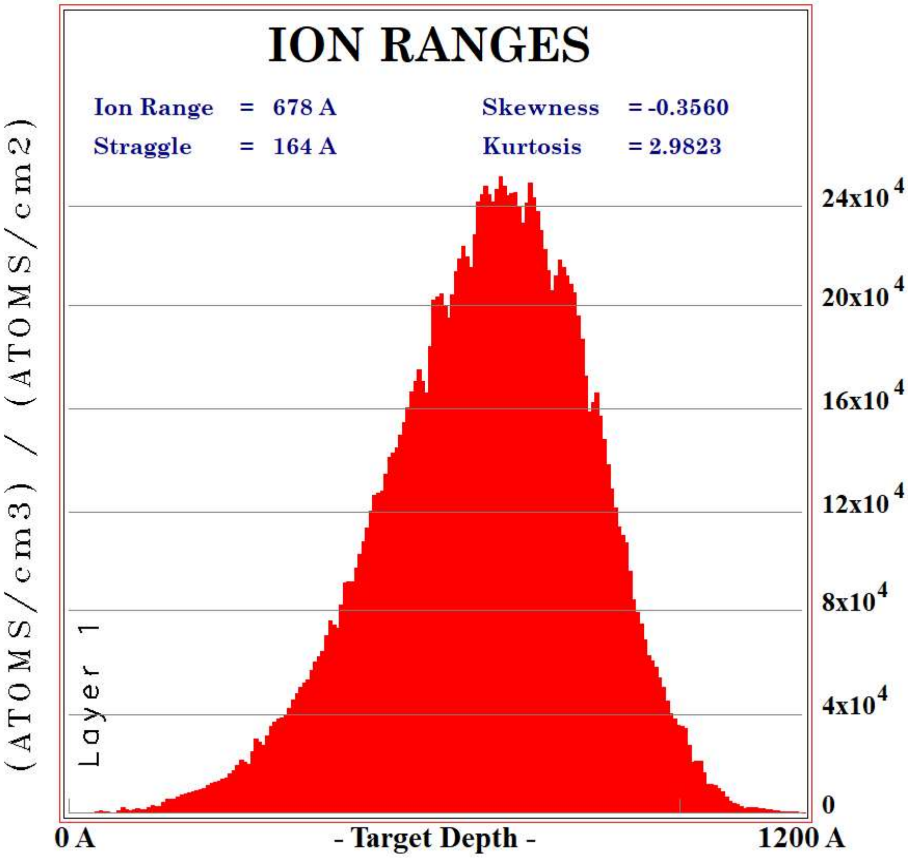

Figure 2.12: Ion range probability distribution calculated from SRIM for 30,000 ^{28}Si^{+} ions in diamond. The ion energy, E_0, is 100 keV.

2.5 Franck-Condon Principle

One of the downsides to the NV center which make it sub-optimal for some bio-applications is its broad spectral features, shown in Figure 2.13(a). We can explain the NV center's broad spectrum using the Franck-Condon principle. Figure 2.13(b) shows a simplified model of the energy levels of the NV center. Two electronic levels corresponding to the ground, and excited state are shown. Each electronic level consists of a manifold of vibrational levels denoted with quantum numbers η, and η' for the ground and excites states respectively. Any given vibrational mode has discrete energies ($\eta, \eta' = 0, 1, 2, 3, 4$) described by a harmonic potential. First, we will describe the spectrum resulting from one mode, then we will generalize to the case of many modes.

According to the Franck-Condon principle the most likely vertical transitions from the ground state are to turning points in the excited state. The turning points

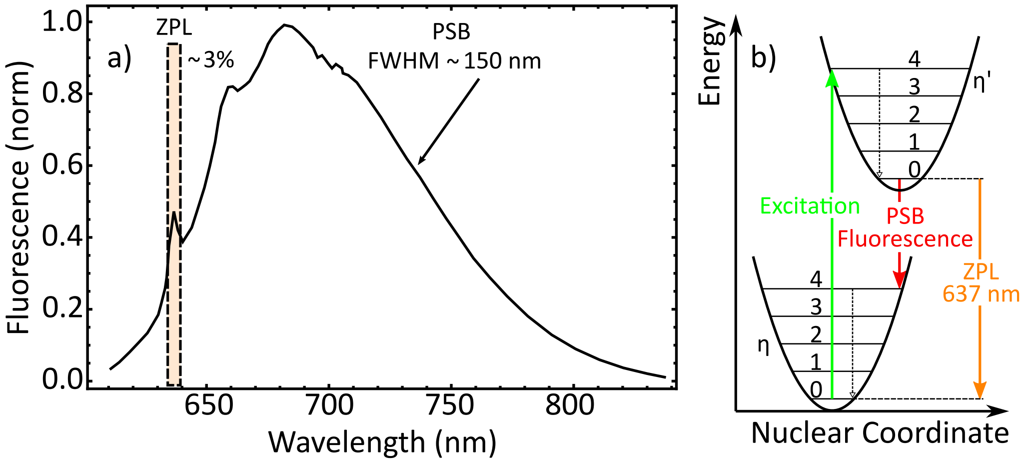

Figure 2.13: (a) NV color center emission spectrum adapted from [41]. The NV center only has roughly 3% of its emission that falls within the zero-phonon line (ZPL) and a wide phonon sideband (PSB) with a FWHM of 150 nm. (b) Diagram illustrating the Franck-Condon principle for the NV center with a single harmonic vibrational mode.

are the end points of the vibrational motion with respect to the nuclear coordinate. According to this principle the most likely transition is from $\eta = 0 \rightarrow \eta' = 4$ for the case shown in Figure 2.13(b). This same principle holds for emission. For example, if the NV center were excited from the ground state to $\eta' = 4$, then it would decay almost immediately to $\eta' = 0$. The most probable transition back to the ground state is then $\eta' = 0 \rightarrow \eta = 4$. This means that the most probably emission frequency is shifted by 4 vibrational quanta with respect to the zero-phonon line ($\eta' = 0 \rightarrow \eta = 0$). This accounts for the large shift between the zero-phonon line, and the phonon sideband ($\eta' = 0 \rightarrow \eta > 0$). Transitions from $\eta' = 0 \rightarrow \eta = 2, 3, 5, 6, ...$ also have a significant probability. This accounts for the broad spectrum of the phonon sideband which has a FWHM of 150 nm.

However, so far we have only considered one vibrational mode and would expect the transitions to be a discrete comb of Dirac delta functions shown in Figure 2.14(a). Because of the finite vibrational decay time $\tau_{\text{vib}} \approx 1$ ps these spectral lines are not idealized Dirac delta functions, they have some linewidth $\approx 1/\tau_{\text{vib}} = 1$ THz. The next correction needed to understand the experimental data is that there is not just one mode, but many vibrational modes. Figure 2.14(b) shows the spectrum with the same 1 THz broadening, but now two different modes, and we can see that the spectrum is beginning to get complicated. Figure 2.14(c) shows the spectrum for 86 different modes, and a histogram of the selected mode spacing is shown in Figure 2.14(d). In this case, the simulated spectrum begins to approximate the experimental spectrum shown in Figure 2.14(c).

Taking a look at the SiV center in the same light, Figure 2.15(b) shows a simplified model of one vibrational mode for the SiV center. The SiV center has a smaller nuclear coordinate shift between the ground, and excited electronic states. Thus, in emission the most likely transition would be from $\eta' = 0 \rightarrow \eta = 1$. This leads to the smaller shift of the phonon sideband with respect to the zero-phonon line.

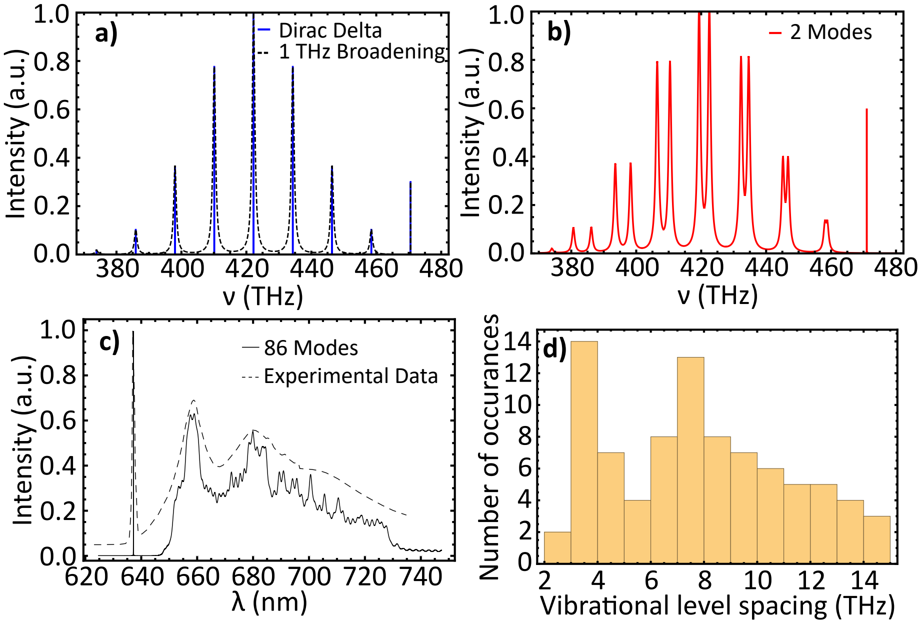

Figure 2.14: (a) Emission spectrum of a single vibrational mode according to the Franck-Condon principle. The blue lines are transitions modeled as Dirac Delta functions. The black dashed line is the same transitions with 1 THz broadening. Each vibrational level is separated by 12.1 THz. (b) Emission spectrum for two different vibrational modes with mode spacing's 12.1 and 10.9 THz (c) Emission spectrum for 86 different vibrational modes. The solid black line is modeled after the Franck-Condon principle as discussed in the text. The black dashed line is experimental data for the negatively-charged NV center at low temperatures, adapted from Doherty *et al.* (2013) [42]. (d) Histogram showing the ground state vibrational level spacing that were used to create the spectrum in (c).

Transitions from $\eta' = 0 \rightarrow \eta > 2$ have a small probability. This accounts for the narrow spectrum of the phonon sideband which has a FWHM of 20 nm, shown in Figure 2.15(a).

Because of its narrow spectral features, we propose using the SiV color center as a more promising alternative for STED microscopy applications. At first look, you may think that this would not be the case when comparing it to the NV color center. We use the phonon sideband to stimulate emission, and the NV center has 97% of its spectrum in the phonon sideband where the SiV only has 30%, which is

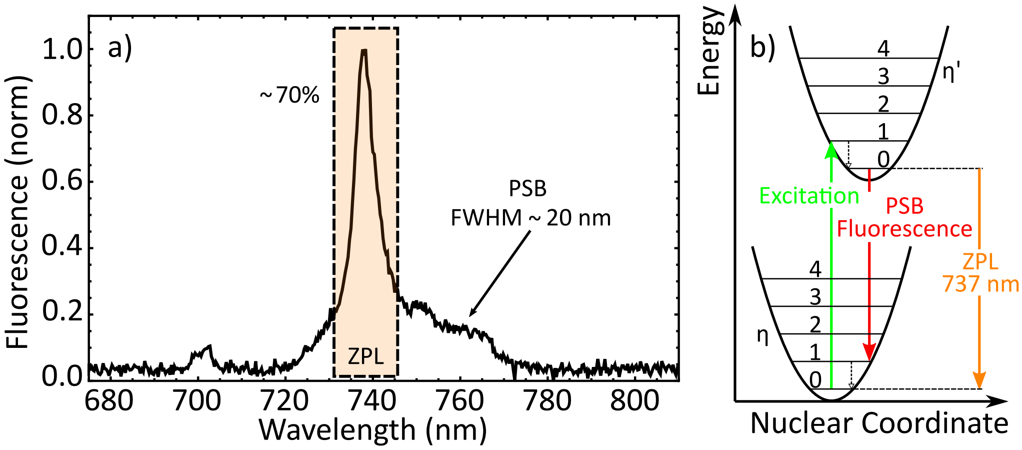

Figure 2.15: (a) SiV color center emission spectrum. The SiV center has roughly 70% of its emission within the ZPL and a narrow PSB with FWHM of 20 nm. (b) Diagram illustrating the Franck-Condon principle for the SiV center with a single harmonic vibrational mode. The shift between the ground and excited state manifolds is much smaller than for the NV center.

a factor of 3 smaller. However, the SiV center's phonon sideband is approximately 7x narrower than the NV center's phonon sideband. If the integrated electric dipole moment were the same for both the NV center and the SiV center, this would suggest the SiV center has a larger stimulated emission cross section when depleting at the peak of the PSB. This observation was part of the motivation for why we studied the STED properties of SiV centers.

2.6 Charge State Instability Near Surfaces

The NV center has been shown to blink in small nanodiamonds. This is due to the NV center changing charge states from the negative charge state to the neutral state, and back again. Recall that most experiments using the NV center are monitoring the fluorescence of the negatively-charged state, so the neutral charge state appears as a dark state. Blinking in nanodiamond can be attributed to a concept called band bending [43–49]. The energy bands of the diamond are bent near the diamond surface. The amount, and direction the bands are bent can be altered due to different surface terminations, and donor or acceptor concentrations [46, 48]. This is usually illustrated with showing the energy levels of the conduction band minimum (E_C), and the valence band maximum (E_V) changing as they approach the surface. When these bands bend, all the energy levels related to them bend as well.

When two different materials come into contact, the interface between the ma-

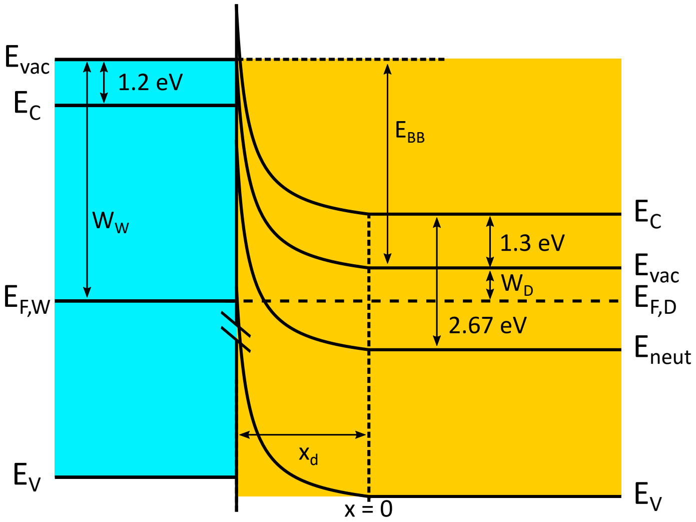

Figure 2.16: Band diagram for diamond containing substitutional nitrogen and NV centers with a hydrogen terminated surface (orange) and water (blue). The energy gap between conduction band minimum (E_C) and valence band maximum (E_V) in diamond is 5.47 eV. The energy required to change the NV from the negative-charge state to the neutral charge state was set at 2.67 eV below the conduction band minimum [50]. Due to the negative electron affinity caused by the hydrogen surface termination, the vacuum level (E_{vac}) lies below the conduction band minimum, within the diamond bandgap. The Fermi level in diamond ($E_{F,D}$) is 1.7 eV below E_C [43]. The work function for diamond is $W_D = 0.4$ eV. The energy gap between E_C and E_V in water is 8.86 eV [51]. E_{vac} is 1.2 eV above E_C for water. The Fermi level of water ($E_{F,W}$) was set at 3.45 eV below E_C [52]. The work function for water is $W_W = 4.65$ eV. The depletion region, x_d at the diamond surface was calculated to be 15 nm from equation (2.36).

terials has a transfer of electrons. The vacuum level (E_{vac}) of the materials must be continuous at the interface due to energy conservation; but, in equilibrium, the Fermi level (E_F) of the whole system is constant. This creates an electric potential causing electrons to transfer across the interface.

To gain an intuition to how this applies to nanodiamonds, we will consider a simple case of water, and bulk diamond illustrated in Figure 2.16. The difference between the vacuum levels of these materials can be calculated with the work functions of the two materials in contact [53]:

$$E_{BB} = |W_W - W_D|, \tag{2.35}$$

where W_W is the work function for water, and W_D is the work function for diamond. The work function is the energy required to move an electron from E_F to E_{vac}. The region where the bands bend significantly is known as the depletion region, x_d, and it can be calculated [54]:

$$x_d = \frac{2\epsilon\epsilon_0|\phi_0|}{ne}, \tag{2.36}$$

where ϵ is the dielectric constant, ϵ_0 is the vacuum permitivity, n is the donor concentration, e is the charge of an electron, and ϕ_0 the electric potential of the diamond away from the depletion region, and is related to the work function of diamond, $\phi_0 = -W_D/e$. The electric potential in the depletion region, $\phi(x)$, can be calculated using Poisson's equation:

$$\frac{d^2\phi(x)}{dx^2} = -\frac{ne}{\epsilon\epsilon_0}. \tag{2.37}$$

Figure 2.16 shows a band diagram for diamond containing NV centers with a hydrogen terminated surface [43]. This diamond has a layer of water at the surface. For simplicity we assume there is no band bending occurring within the water. The hydrogen terminated surface creates a layer near the surface of the diamond with a negative electron affinity which depletes electrons [55]. A negative electron affinity

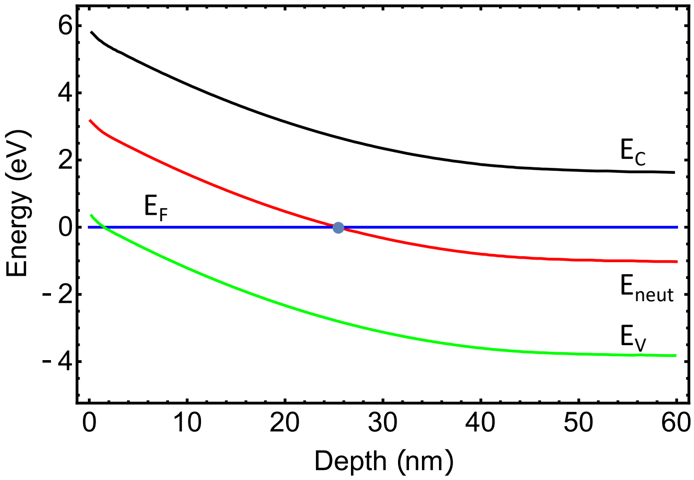

Figure 2.17: Band diagram for diamond containing substitutional nitrogen and NV centers with a hydrogen terminated surface. The energy gap between conduction band minimum (E_C) and valence band maximum (E_V) in diamond is 5.47 eV. The energy required to change the NV from the negative-charge state to the neutral charge state (E_{neut}) was set at 2.67 eV below the conduction band minimum [50]. The Fermi level (E_F) was set to 0 eV for convenience. The gray dot at 25 nm is the point where the energy required to neutralize a negatively-charged NV center is the same as E_F, meaning it has 50% chance to neutralize. A mono layer of water is present on the surface of the diamond to further enhance the band bending for this graph. Image adapted from Newell *et al.* (2016) [43].

causes E_{vac} to fall below E_C. E_{neut} is the energy required to change the NV from the negative charge state to the neutral charge state. It depends on where the ground state energies lie within the bandgap for both the neutral and negative NV charge state [50]. Away from the depletion region ($x \geq 0$), E_{neut} is below E_F, and the NV center is more likely to be in the negative charge state. At some location within the depletion region ($-x_d < x < 0$), E_{neut} crosses E_F, and the neutral charge state becomes more likely.

So far, we have only discussed a very simple picture for diamond, and water. Figure 2.17 shows a more accurate band bending diagram for the same diamond as before, but calculated numerically using a finite element method [43]. This model

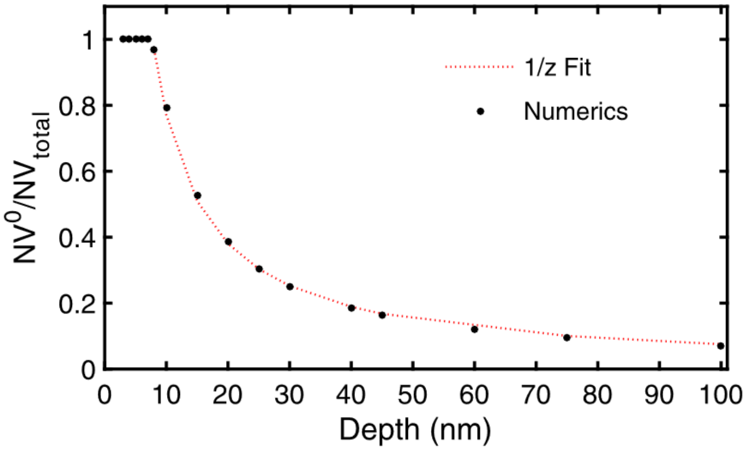

Figure 2.18: Depth dependence of the negatively-charged NV center neutralization. A Gaussian profile, with peak concentration of 10^{20} cm^{-3} and standard deviation 0.5 nm, was used to evaluate neutralization at each depth. The dotted line represents a $1/z$ fit to the data points and suggests the major force driving the neutralization of the negatively-charged NV center is electrostatic. Image from Newell *et al.* (2016) [43].

uses a nonlinear Poisson equation for bulk diamond, Schrödinger-Poisson equation in the depletion region, and a Poisson-Boltzman equation in the water layer.

Figure 2.18 shows the depth dependence of the ratio of neutral NV centers to total NV centers [43]. As the NV centers get closer to the surface the negative charge state is less stable. The plateau region in Figure 2.18 occurs when the potential difference, ϕ, generated by the depletion layer near the surface becomes greater or equal to the total energy required to neutralize all the negatively-charged NV centers at that depth.

The SiV center has shown to be stable in nanodiamonds smaller than 2 nm [20]. The stability of the SiV center likely comes from E_{neut} for the SiV center being well below E_F, causing it to cross E_F closer to the surface of the diamond. The stability of the SiV center in smaller nanodiamonds makes it a promising candidate for use as a fluorescent label in super resolution microscopy.

2.7 Optical Nonlinearities

The same optical properties that make the SiV center a promising candidate for use in biological imaging, make it a good candidate to mediate light-matter interactions for nonlinear optics applications. We propose the SiV center be used in nanophotonic devices for optical switching. An optical switch can be made using nonlinear properties of light in matter, such as saturable absorption. Saturable absorption is a property of materials where the absorption of light decreases as the intensity of the excitation light increases. This happens when the atoms in the ground state of the material are excited to the excited state, and do not have enough time to decay before the ground state population is completely depleted.

A saturable absorber can be used as a switch in a pump-probe type of experiment. Consider a single atom with two energy levels, as shown in Figure 2.19. When a single photon level probe pulse interacts with the atom, the atom absorbs the light, and there is no transmission of the probe. We label this as the switch's "OFF" state. However, if just before the probe passes, a resonant optical pump pulse initialized the atom into the excited state, the atom cannot absorb the probe and it is transmitted through. This is labeled as the switch's "ON" state. This single-atom switch only

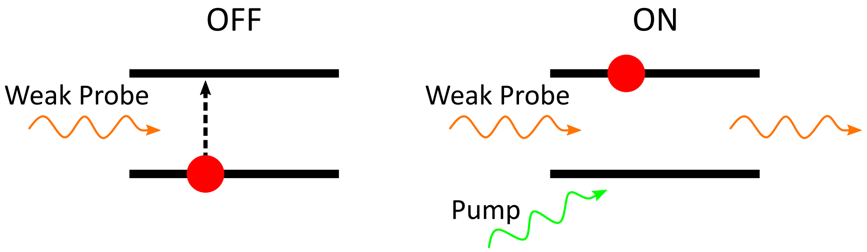

Figure 2.19: Diagram showing how a single-atom saturable absorber can be used as a switch. On the left, there is no pump pulse to initialize the atom to the excited state, causing the weak probe beam to be absorbed and no transmission. On the right, the pump pulse depletes the ground state, causing the weak probe beam to transmit completely.

requires one photon to be absorbed in order to switch from "OFF" to "ON".

In our case, the material is diamond doped with SiV centers. Each individual SiV center has a slightly different optical transition frequency depending on its immediate electrostatic environment. If we were to make many devices, each with a single SiV center, the devices would all have a different absorption spectrum. Thus, if we chose a single frequency for the control pump, and probe, the switching behavior will be different from device to device. This is not desirable for a scalable network where ideally all the switches would behave identically. If instead we put an ensemble of SiV centers in each device, such that every device had a similar absorption spectrum, we could ensure that each device had similar switching behavior.

To illustrate this concept, we consider a single device fabricated from diamond with a SiV center density of roughly 10^{14} SiV/cm^3, and a volume of 2.5×10^{-12} cm^3. Such a device can be expected to have about 250 SiV centers. Figure 2.20 shows the emission spectrum for a device with 250 SiV centers. Each SiV center's absorption

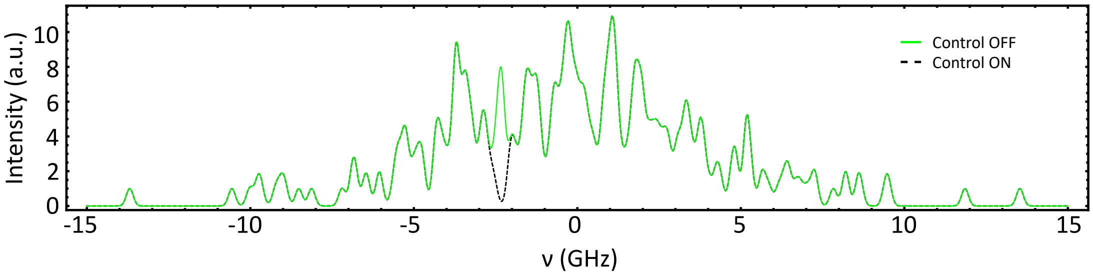

Figure 2.20: Emission spectrum of 250 SiV centers. The emission is centered at the ZPL of the SiV center, 406.464 THz. The distribution of the SiV center's central frequency is according to a Gaussian probability distribution with a FWHM of 10 GHz. Each SiV center has 250 MHz homogeneous broadening. In green is the "OFF" state, where all 250 SiV centers are absorbing photons from the probe. The black dotted line represents the "ON" state where the 9 SiV centers in that region have been turned off. The hole was burnt into the spectrum at a frequency detuned to -2.38 GHz, which turns off SiV centers in that spectral region within 125 MHz of the detuning. The contrast in the spectral hole is 97%.

spectrum is assumed have a Gaussian linewidth with a FWHM of 250 MHz (homogeneous broadening). The central frequency of these absorption spectra are given by sampling a Gaussian probability distribution with a FWHM of 10 GHz (inhomogeneous broadening). The expected absorption spectrum for one possible sampling of the Gaussian probability distribution is shown as green in Figure 2.20.

Now suppose a control pump pulse, with detuning of -2.38 GHz from the central frequency, is applied. We assume it depletes the ground state of all SiV centers that have a central frequency within 125 MHz of the control pump optical frequency. In this case, the expected absorption spectrum is shown as a black dotted line in Figure 2.20. Notice the spectra with and without the control beam are similar, except there is a hole in the absorption spectrum in the case with the control pump pulse applied. This process is known as spectral hole burning. The contrast of this hole in the spectra is 97%. In this example, the pump pulse depleted 9 SiV centers,

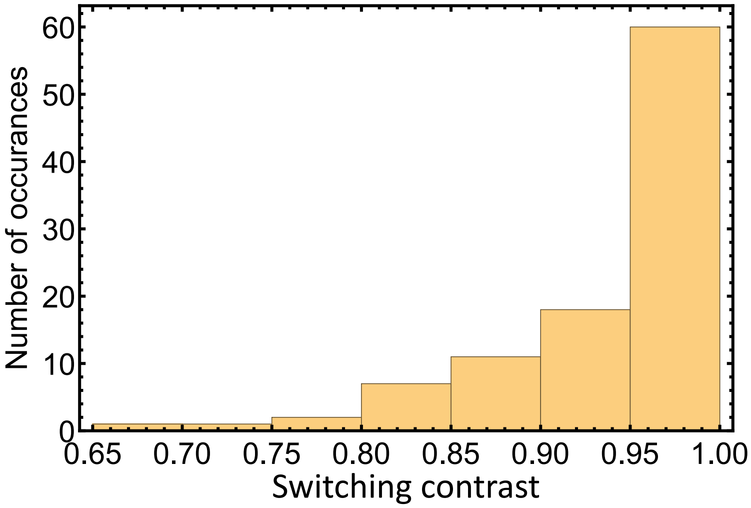

Figure 2.21: Histogram showing the switching contrast for 100 different devices each containing 250 SiV centers as shown in Figure 2.20. Each device simulated has the optical transition frequencies randomly assigned by sampling a Gaussian probability distribution with a FWHM of 10 GHz. The optical frequency of the pump beam was kept constant across all 100 simulations.

so a minimum of 9 absorbed photons are required from the pump pulse. This has implications for the power consumption for such a device.

Figure 2.21 shows the switching contrast for 100 different simulated devices. In this case, we assume that the control pump pulse depletes 9 SiV centers that have optical transition frequencies near the pump optical frequency. We found that 78% of the devices had a switching contrast of 90% or greater.

In order for these sorts of devices to be useful in a scalable platform, it would be important that nearly all of the control pump photons are absorbed. To increase this absorption probability we propose to use nanophotonic cavities that enhance the SiV-light interaction.

Chapter 3

Experiment

This chapter was taken and adapted from reference [56].

3.1 Introduction

Stimulated emission depletion (STED) microscopy is one of several techniques which can image fluorescent molecules with a spatial resolution superior to the optical diffraction limit [28, 57]. While the resolution in STED microscopy can theoretically approach the scale of individual atoms [58], resolving structures at the few nanometer scale in biological samples remains an experimental challenge. This is partly due to a lack of fluorescent probes which possess the requisite photophysical properties and are sufficiently small, bright, photostable, and non-toxic.

In STED microscopy, the theoretical lateral resolution, Δd, scales approximately as $\Delta d \propto \sqrt{I_{\text{sat}}/I}$, where I is the optical intensity used to stimulate emission and I_{sat} is the fluorophore's stimulated-emission saturation intensity [59]. This scaling has two consequences for probe design. The first is that a low I_{sat} is desirable so that low enough values of I can be used to avoid sample photodamage while maintaining high resolution. The second consequence is that a high degree of photostability is required to simultaneously realize low values of Δd and a high fluorescence signal amplitude. This is because, when I_{sat}/I is small (as needed for high resolution), many fluorophore absorption events do not produce detectable fluorescence, yet they often have the same propensity for photobleaching [60]. Thus, if the fluorophore bleaches after a fixed number of absorption events, there is an unavoidable trade off between spatial resolution and fluorescence signal amplitude. A similar argument holds in pulsed STED microscopy, where the STED beam's pulse fluence is substituted for intensity.

Organic dye molecules are among the most widely used fluorophores in STED microscopy [61]. They can be functionalized to specifically bind to biological targets [62] and are relatively non-toxic [63]. They also can produce high fluorescence rates [64] and feature sufficiently low values of I_{sat} [65] to enable imaging of cells with a spatial resolution down to ∼20 nm [66]. Nevertheless, standard organic fluorophores suffer from photobleaching due to irreversible chemical reactions [67], thereby limiting the achievable fluorescence signal amplitude and resolution [68].

Solid-state color centers are an intriguing alternative probe for STED microscopy, as the host crystal prevents some forms of photobleaching [69]. For example, the negatively-charged nitrogen vacancy (NV) color center in diamond exhibits nearly perfect photostability in nanodiamonds with characteristic dimensions down to ∼10 nm [70]. Moreover diamond is a relatively non-toxic host crystal that can be functionalized to bind to intracellular targets [71]. NV centers in bulk diamond have been used to set record spatial resolutions in STED microscopy, with lateral resolutions as small as $\Delta d = 2.4$ nm [72]. However, NV centers have some limitations in their use in STED microscopy. The fluorescence intensity of a single NV center is more than an order of magnitude weaker than a typical organic fluorophore [73] under similar conditions. They require high stimulated emission depletion intensities, owing to

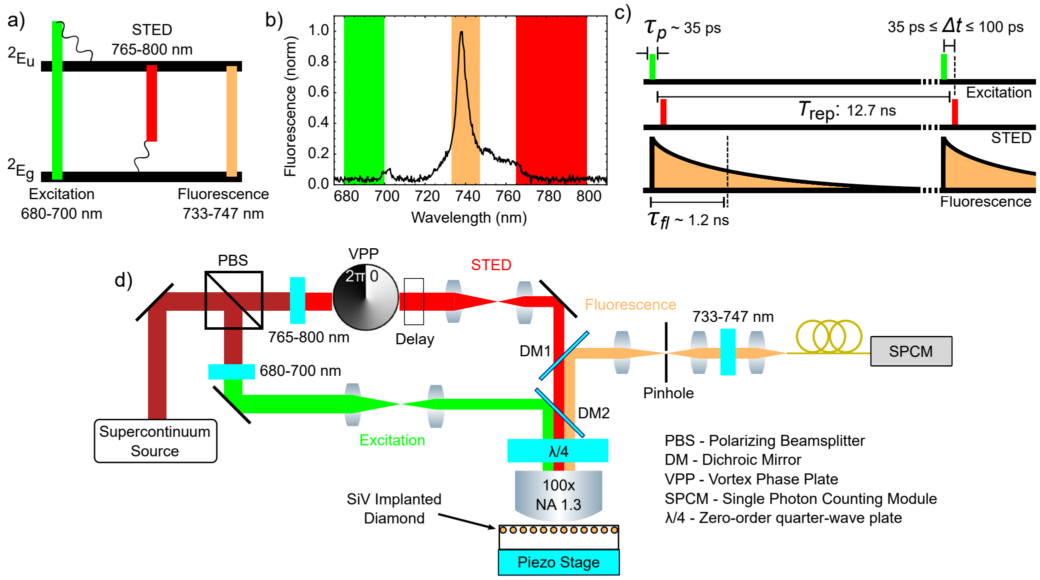

Figure 3.1: **SiV STED methodology.** (a) SiV optical transitions between the ground (^2E_g) and excited (^2E_u) electronic states [79, 80]. (b) SiV fluorescence spectrum under 685-nm excitation. The bands used for excitation, fluorescence collection, and STED, are labeled in green, orange, and red, respectively. The wavelength band of the STED beam (765–800 nm) was selected to maximize the available power from the supercontinuum source, while minimizing anti-Stokes excitation (Sec. SVII) and remaining within the tail of the phonon sideband. (c) Pulse sequence used for STED microscopy and for measuring the SiV stimulated emission cross section. The pulses are provided by a picosecond supercontinuum source with a repetition rate of 78 MHz. (d) Apparatus used for STED microscopy of SiV centers. An oil-immersion microscope objective with numerical aperture NA = 1.3 focuses light onto, and collects fluorescence from, SiV centers. Additional details are found in Sec. SI.

their relatively low cross section (approximately 1–2 × 10^{-17} cm^2 [74, 75]) and their propensity for excited state absorption [76, 77]. Finally, NV centers tend to blink in small nanodiamonds and do not produce observable fluorescence in nanodiamonds smaller than ∼10 nm [70, 78].

Negatively-charged silicon vacancy (SiV) color centers in diamond may offer a more promising alternative for STED microscopy applications. SiV centers have been shown to be photostable in nanodiamonds as small as ∼2 nm [20], and their fluorescence spectrum lies in a narrow band in the near infrared [30]. Here, we report measurements of the stimulated emission cross section of SiV centers in bulk diamond. We find $\sigma_{\mathrm{STED}} = (4.0 \pm 0.3)\times 10^{-17}$ cm^2 for 765–800 nm light. This is approximately 2–4 times larger than the σ_{STED} reported for NV centers and nearly as large as that of organic fluorophores commonly used in STED microscopy [81,82]. We demonstrate STED microscopy on isolated SiV centers in diamond, realizing a resolution $\Delta d = 89 \pm 2$ nm, limited by the available STED laser pulse energy (0.4 nJ). If these properties are similar in sub-10-nm nanodiamonds, and higher STED pulse energies are available, SiV centers may be ideal probes for high resolution STED microscopy in biological systems. Our methods can also be applied to resolving nanoscale SiV center arrays in quantum information applications [83,84].

3.2 Experimental Setup

The SiV optical transitions and emission spectrum are shown in Figs. 3.1a and 3.1b, respectively. The pulse sequence used for STED microscopy is shown in Fig. 3.1c. A laser pulse (680–700 nm) excites SiV centers on their absorption phonon sideband. A second pulse (765–800 nm), with a time-delay of 35 ps $\lesssim \Delta t \lesssim 100$ ps (Sec. SIV), stimulates SiV emission on the emission phonon sideband. Fluorescence is collected about the SiV zero-phonon line (ZPL) in the band 733–747 nm. Both excitation and stimulated emission pulses have a temporal full-width-at-half-maximum (FWHM), $\tau_p \approx 35$ ps (Sec. SIV), that is considerably shorter than the SiV excited state lifetime ($\tau_{fl} \approx 1.2$ ns [30]). The sequence is repeated after the laser repetition time, $T_{rep} = 12.7$ ns $>> \tau_{fl}$, which is long enough to ensure SiV centers are initialized in their ground state at the start of each sequence.

A schematic of our SiV STED microscope is shown in Fig. 3.1d. A supercontinuum source is used to generate both excitation and stimulated emission pulses. The

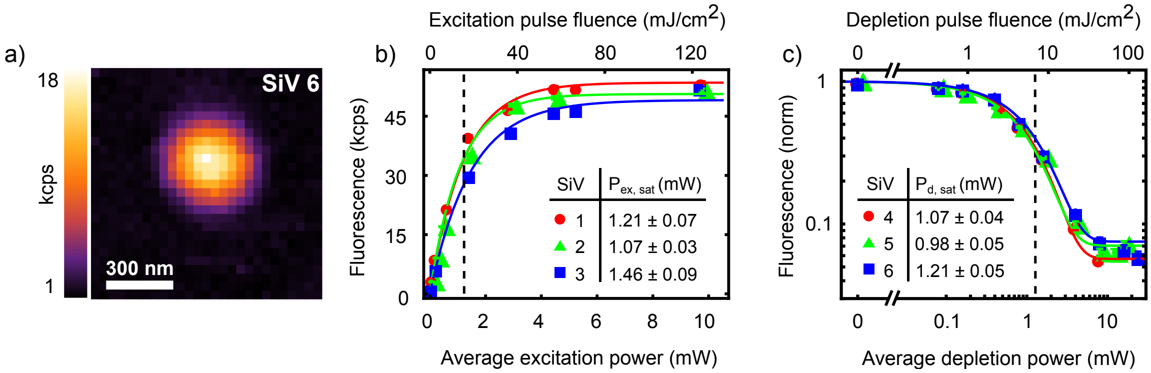

Figure 3.2: **Excitation and depletion saturation curves.** (a) Confocal image of ZPL emission (733–747 nm) from an isolated SiV center excited with 680–700 nm light. (b) Fluorescence intensity as a function of average excitation power (or corresponding peak pulse fluence) for three SiV centers. Inset: table reporting fitted average excitation saturation powers and fit uncertainties for each SiV center. The mean value is annotated as a dashed line on the plot. (c) Normalized fluorescence intensity as a function of average depletion power (or corresponding peak pulse fluence) for three different SiV centers excited at $P_{\text{ex}} \approx P_{\text{ex, sat}}$. Inset: table reporting fitted average depletion saturation powers and fit uncertainties for each SiV center. The mean value is annotated as a dashed line on the plot.

SiV centers studied here were formed from ion implantation and annealing. They were typically ∼50 nm below the diamond surface with an approximate areal density of 10^6–10^8 cm^{-2}. Section 4.2 contains additional details on the samples and how they were prepared.

3.3 Results

Figure 3.2a displays a confocal image of ZPL emission (733–747 nm) from an isolated SiV center under 680–700 nm excitation. The FWHM of the feature is ∼270 nm, consistent with the diffraction limit of our microscope. Such isolated features were assumed to be single SiV centers based on their sparsity and nearly identical intensity, Sec. SVI. Figure 3.2b shows the detected fluorescence intensity of three SiV centers as a function of average excitation power, P_{ex}. We fit these data to a saturation curve of the form $C = C_{\max}(1 - \mathrm{e}^{-P_{\mathrm{ex}}/P_{\mathrm{ex,\,sat}}})$ [85], where $C_{\max}$ is the peak detected fluorescence intensity [typically 45 to 55 kilocounts/second (kcps) for SiV centers in our setup] and $P_{\mathrm{ex,\,sat}}$ is the average excitation saturation power. From the fits, we extract $P_{\mathrm{ex,\,sat}} = 1.2 \pm 0.2$ mW, corresponding to the mean and standard deviation for the set of three SiV centers. By incorporating the laser repetition rate and independently-measured intensity profile of the excitation spot (Sec. SIII), this value converts to a saturation pulse fluence $F_{\mathrm{ex,\,sat}} = 15 \pm 3$ mJ/cm^2.

The excitation cross-section for this wavelength band is then calculated (Sec. SIII) as $\sigma_{\mathrm{ex}} = E_{\mathrm{ph,\,ex}}/F_{\mathrm{ex,\,sat}} = (1.8 \pm 0.3) \times 10^{-17}$ cm^2, where $E_{\mathrm{ph,\,ex}} = 2.9 \times 10^{-19}$ J is the excitation photon energy. All remaining experiments were performed with average excitation power $P_{\mathrm{ex}} \lesssim P_{\mathrm{ex,sat}}$.

We determined the stimulated emission cross section for 765–800 nm light, σ_{STED}, using the pulse sequence in Fig. 3.1c with overlapped Gaussian spatial profiles for excitation and depletion beams. Figure 3.2c shows the normalized fluorescence intensity from three SiV centers as a function of average depletion power, P_{d}. These data were fit to an exponential decay function, $C \propto \mathrm{e}^{-P_{\mathrm{d}}/P_{\mathrm{d,\,sat}}}$, revealing an average depletion saturation power $P_{\mathrm{d,\,sat}} = 1.1 \pm 0.1$ mW (mean and standard deviation for the three SiV centers). This power corresponds to a depletion saturation pulse fluence $F_{\mathrm{d,\,sat}} = 6.8 \pm 0.6$ mJ/cm^2 (Sec. SIII). The stimulated emission cross section is therefore $\sigma_{\mathrm{STED}} = E_{\mathrm{ph,\,d}}/F_{\mathrm{d,\,sat}} = (4.0 \pm 0.3) \times 10^{-17}$ cm^2 (Sec. SIII), where $E_{\mathrm{ph,\,d}} = 2.5 \times 10^{-19}$ J is the depletion photon energy. This cross section is approximately 2-4 times larger than that of the diamond NV center [74, 75] and approaches that of the organic dye molecules, (3–15) $\times 10^{-17}$ cm^2 [81, 82], commonly used in STED microscopy.

We next show that STED microscopy applied to SiV centers can be used to realize resolution beyond the optical diffraction limit. We continue to use the pulse sequence

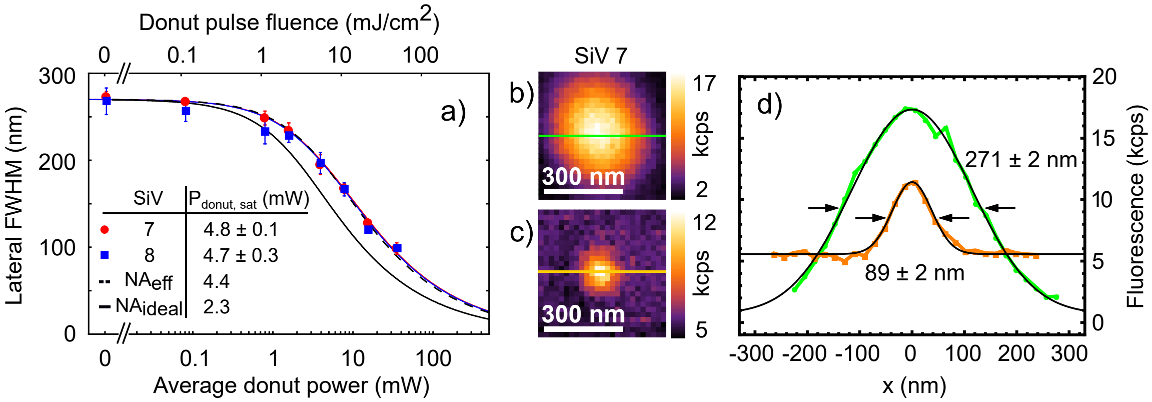

Figure 3.3: **STED resolution enhancement.** (a) Lateral FWHM of STED profiles of two isolated SiV centers as a function of average donut power (or corresponding peak pulse fluence). Solid red and blue lines are fits to Eq. (3.1) with fitted average donut saturation powers given in the inset. Solid and dashed black lines are the theoretical resolution (Sec. SV) for an ideal donut profile ($\text{NA}_{\text{ideal}} = 1.3$) and the experimentally-measured donut profile ($\text{NA}_{\text{eff}} = 1.1$), respectively. A lateral FWHM of ∼20 nm is expected at $P_{\text{donut}} = 400$ mW, which corresponds to a pulse energy (5 nJ) commonly used in STED microscopy [86]. (b) Confocal and (c) STED image of an isolated SiV center taken at $P_{\text{donut}} = 32$ mW (0.4 nJ pulse energy). Annotated linecuts are plotted in (d). The FWHM of the confocal profile (green) is reduced by a factor of three when applying the STED donut beam (orange). Black curves in (d) are Gaussian fits and annotated values are their fitted FWHM.

in Fig. 3.1c, but now a vortex phase plate is inserted in the STED path to shape its spatial profile into a donut. We recorded STED images of isolated SiV centers at varying donut powers, P_{donut}. Each image is fit to a two-dimensional Gaussian profile to extract the SiV lateral FWHM (Sec. SV). At least three images were acquired for each SiV center at each power to determine statistical uncertainty. The results are plotted in Fig. 3.3a. Example images taken at $P_{\text{donut}} = 0$ and $P_{\text{donut}} = 32$ mW (0.4 nJ pulse energy) are shown in Figs. 3.3b and c, respectively. The intensity profiles of linecuts through the center of the images are displayed in Fig. 3.3d. The FWHM of the confocal image linecut ($P_{\text{donut}} = 0$) is 271 ± 2 nm, consistent with the diffraction-limited resolution of our confocal microscope. At $P_{\text{donut}} = 32$ mW, near the highest power available in our setup, the FWHM shrinks by a factor of ∼3 to

$\Delta d = 89 \pm 2$ nm. At this power, we observe a ~2-fold reduction in peak fluorescence intensity (see Fig. S5), likely because of imperfect donut contrast. We also observe a slight increase in background due, in part, to anti-Stokes fluorescence (Sec. SVII).

The data in Fig. 3.3a were fit to a commonly-used approximation for STED resolution [87]:

$$\Delta d(P_{\text{donut}}) \approx \frac{D}{\sqrt{1 + \frac{P_{\text{donut}}}{P_{\text{donut, sat}}}}}. \tag{3.1}$$

Here D is the confocal microscope resolution, which we set to $D = 270$ nm based on independent measurements, and $P_{\text{donut, sat}}$ is a fitted characteristic power that satisfies $\Delta d(P_{\text{donut, sat}}) = D/\sqrt{2}$. From the fits (solid red and blue curves), we extract $P_{\text{donut, sat}} = 4.8 \pm 0.1$ and 4.7 ± 0.3 mW for two different SiV centers. These powers correspond to characteristic peak pulse fluences of 9.7 ± 0.2 and 9.5 ± 0.6 mJ/cm^2, respectively (Sec. SV).

The theoretical resolution for a perfect donut beam focused with a $\text{NA}_{\text{ideal}} = 1.3$ objective (solid black line in Fig. 3.3a) is approximated from a numerical model (Sec. SV) incorporating the previously measured $\sigma_{\text{STED}} = 4 \times 10^{-17}$ cm^2. The corresponding saturation power for this ideal case is $P_{\text{donut, sat}} = 2.3$ mW, approximately two times smaller than the observed value. Experimentally, we measure a donut beam profile that is more consistent with an effective numerical aperture of $\text{NA}_{\text{eff}} = 1.1$. This may be due to wavefront or polarization distortions of the STED beam and/or under-filling of the beam at the objective's back aperture (see Sec. SV). Incorporating this NA into the numerical model (dashed black line in Fig. 3.3a), we find excellent agreement with the experimental resolution. The corresponding saturation power, $P_{\text{donut, sat}} = 4.4$ mW, is consistent with the fits to Eq. (3.1).

Finally, we used STED microscopy to resolve SiV centers spaced closer than the optical diffraction limit. Figure 3.4 compares confocal and STED images of SiV clusters in two different high-SiV-density regions (Sec. SII). Unlike the confocal images (Figs. 3.4a,b), the STED images (Fig. 3.4c,d) clearly resolve SiV centers separated by $\lesssim$150 nm. Taking into account the similar brightness and FWHM of features in the STED images (see Sec. SVI), it is likely that each individual SiV center in the scan region is resolved. Figure 3.4e shows linecuts through a subregion containing closely-spaced SiV centers (dashed lines in Fig. 3.4b,d). While the confocal image contains little information about the SiV locations, Gaussian fits to the STED linecut reveal two SiV centers separated by 154 ± 2 nm.

3.4 Discussion and conclusion

The demonstration of super-resolution STED microscopy with SiV centers has implications for several applications. Importantly, all SiV centers studied here showed perfect photostability (no blinking or bleaching), even under continuous illumination with high STED intensity for several days. However, future work is needed to validate the utility of SiV STED microscopy in biological samples. The modest resolution realized here (~90 nm) was limited by the maximum STED pulse energy (~ 0.4 nJ) available in our setup. If a realistic pulse energy of 5 nJ was used, the resolution would improve to $\Delta d \approx 20$ nm for an optimized STED beam profile (Fig. 3.3a). This compares favorably to the STED resolution realized with organic dye molecules ($\Delta d \approx 35$ nm) under similar conditions [86, 88].

Widespread adoption of SiV probes in STED microscopy will also require development of high-yield methods for fabricating monodisperse sub-10-nm SiV-doped nanodiamonds [89]. If SiV centers in these nanodiamonds have similar photophysical properties as in bulk diamond, as suggested in prior work [20, 90, 91], they may be ideal probes for super-resolution biological imaging. SiV STED microscopy may also be adapted for super-resolution thermal imaging [92, 93] or multiphoton microscopy [91]. In addition, our microscope is well suited for the study of nanoscale

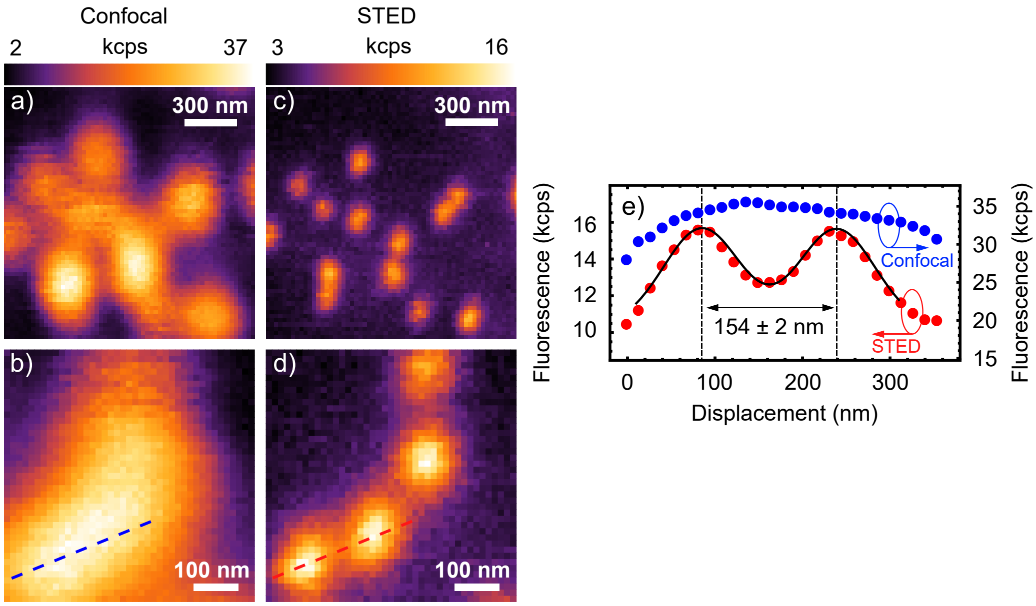

Figure 3.4: **Resolving SiV Clusters in Diamond.** (a,b) Confocal and (c,d) corresponding STED images ($P_{\mathrm{donut}} = 32$ mW) of SiV clusters in two different high-SiV-density regions. The pixel dwell time was 0.1 s. For (a,c) the total image acquisition time was 6 minutes, and for (b,d) it was 3 minutes. (e) Linecuts of the confocal (blue) and STED (red) images across the dashed lines annotated in (b) and (d), respectively. The black solid line is a fit to two Gaussian functions, revealing a SiV center separation of 154 ± 2 nm.

arrays of SiV centers for applications in quantum information [83, 84].

In summary, we demonstrated that SiV centers can be used as photostable fluorophores in STED microscopy. We determined the SiV stimulated-emission cross section for 765–800 nm light to be $\sigma_{\mathrm{STED}} = (4.0 \pm 0.3)\times 10^{-17}$ cm^2, a factor of 2–4 larger than that of NV centers and approaching that of common organic dye molecules. Our results hold promise for future applications in biological imaging and quantum information.

Chapter 4

Supplemental Information

This chapter was taken and adapted from the supplemntal information for reference [56].

4.1 Microscope setup

A detailed diagram of the STED microscope is shown in Fig. 3.1d in the main text. Here we provide additional details. A supercontinuum fiber laser (SuperK EXTREME EXR-20, NKT Photonics) provides a train of picosecond optical pulses with a repetition rate ($1/T_{rep} = 78$ MHz). A polarizing beamsplitter (PBS202, Thorlabs) splits the supercontinuum light into two paths (one for excitation, the other for STED) with orthogonal linear polarizations. Spectral filters are used to select the desired excitation and STED wavelength bands. For excitation (680–700 nm), a combination of a band-pass filter (FB700-40, Thorlabs) and short-pass filter (FES0700, Thorlabs) are used. For the STED path (765–800 nm), a combination of a tunable long-pass filter (TL01-290-25x36, Semrock) and short-pass filter (FES0800, Thorlabs) are used. Both beams are expanded and collimated to fill the back aperture ($\sim$ 6 mm diameter) of an oil-immersion microscope objective (UPLFLN 100x /1.3NA, Olympus) which has $\sim$ 80% transmission for 680–800 nm light. Dichroic mirrors DM2 (T720lpxr, Chroma) and DM1 (FF765-Di01-25x36x2.0, Semrock) are used to re-combine the excitation and STED beams and reflect away the ZPL emission, as indicated in Fig. 3.1d. For STED microscopy, a 0–2π vortex phase plate (VPP-1b, RPC Photonics) is placed in the STED path to generate a donut-shaped intensity profile. A quarter-wave plate (WPQ10ME-780, Thorlabs) placed immediately before the objective lens ensures that the STED beam is right-hand circularly polarized. This polarization preserves the azimuthal symmetry of the donut beam under high-NA focusing [39].

Sample fluorescence was collected by the same objective lens, reflected to the emission path by DM1, and focused by a 200-mm focal length tube lens (ITL200, Thorlabs) onto a 75-μm-diameter pinhole (P75H, Thorlabs). The diameter of the pinhole was selected to be approximately equal to the diameter of the ZPL emission Airy disc in the pinhole image plane. Light exiting the pinhole was re-collimated with a lens and passed through a 740 ± 6.5 nm bandpass filter (FF01-740/13, Semrock) to isolate SiV ZPL emission (733–747 nm). The light was then focused by another lens into a multi-mode fiber (M31L01, Thorlabs) and detected by an avalanche photodiode (SPCM-AQRH-13-FC, Excelitas). The detector output was connected to the counter input of a data acquisition card (NI USB-6363, National Instruments). Three-dimensional scanning of the sample was achieved by a piezo-nanopositioning stage (TRITOR 101 SG, Piezosystem Jena). To form images, the sample scanning was synchronized with the photon counter via the same data acquisition card. The entire sequence was controlled by a home-built LabVIEW program.

4.2 Sample Preparation

The two samples used in this study were electronic grade diamond substrates grown by chemical vapor deposition. The substrates were cleaned in a tri-acid mixture (1:1:1, nitric:perchloric:sulfuric acids) at 200C and subsequently implanted with silicon ions ($^{28}\mathrm{Si}^{+}$) with a dose of 3×10^{9} ions/cm^{2} at an energy of 100 keV, leading to a $\sim$ 50 nm implantation depth. The implanted samples were then annealed for 4 hours at 800C and 2 hours at 1100C in a vacuum furnace [94, 95]. After annealing, one sample had an areal SiV density of $\sim 10^{6}$ cm^{-2}, while the other had a SiV density of $\sim 10^{8}$ cm^{-2}. The lower-density sample was used for experiments shown in Figs. 3.2 and 3.3, while the higher-density sample was used for experiments shown in Fig. 3.4. When excited with $\sim$ 1 mW of 680–700 nm light, both samples exhibited a relatively low and uniform background of 1–2 kcps in regions without SiV centers.

4.3 Pulse fluence and cross section calculations

In order to convert the measured optical power of excitation and depletion beams (P_{ex} and P_d, respectively) to a pulse fluence (F_{ex} and F_d, respectively), detailed knowledge of the beam profiles in the focal plane is required. For the circular Gaussian profile beams used in Fig. 3.2, the peak pulse fluences are given by:

$$F_{ex} = \frac{P_{ex}\, T_{\mathrm{rep}}}{2\pi c_{ex}^{2}}, \tag{4.1}$$

$$F_{d} = \frac{P_{d}\, T_{\mathrm{rep}}}{2\pi c_{d}^{2}}, \tag{4.2}$$

where $T_{\mathrm{rep}} = 12.7$ ns is the laser repetition period, and c_{ex} and c_d are the standard deviations of the Gaussian focal-plane spatial profiles for excitation and depletion beams, respectively.

To determine c_{ex}, scanning confocal fluorescent images of isolated SiV centers were recorded, Fig. 4.1a. Here the pinhole was removed from the emission path to faithfully image the beam profile. The SiV centers were excited by 680–700 nm light at a power below saturation. Several images were recorded and fit to circular Gaussian profiles, revealing $c_{ex} = 127 \pm 2$ nm.

To determine c_d, scanning confocal fluorescent anti-Stokes images (again with pinhole removed) of individual fluorescent beads (Infrared fluorescent 715/755, 0.1 μm FluoSpheres, ThermoFisher Scientific F8799) were recorded, Fig. 4.1b. The beads were diluted and spread on a cover-slip, then excited by the Gaussian depletion beam (765–800 nm) at low power (20 μW). Gaussian fits to several bead images revealed $c_d = 182 \pm 8$ nm.

The one-photon absorption cross sections for excitation and stimulated emission are defined as:

$$\sigma_{\mathrm{ex}} = \frac{E_{\mathrm{ph,\,ex}}}{F_{\mathrm{ex,\,sat}}}, \tag{4.3}$$

$$\sigma_{\mathrm{STED}} = \frac{E_{\mathrm{ph,\,d}}}{F_{\mathrm{d,\,sat}}}, \tag{4.4}$$

where $E_{\mathrm{ph,\,ex}}$ and $E_{\mathrm{ph,\,d}}$ are the excitation and depletion photon energies, $F_{\mathrm{ex,\,sat}}$ is the saturation peak pulse fluence of the excitation beam (corresponding to relative excited-state population of $1 - 1/e$), and $F_{\mathrm{d,\,sat}}$ is the saturation peak pulse fluence of the depletion beam (corresponding to relative excited-state population of $1/e$).

Using the excitation saturation powers obtained for the three SiV centers shown in Figure 3.2b, three different values for the excitation cross section (σ_{ex}) were calculated, Eq. (4.3). The mean value and standard deviation are $\sigma_{\mathrm{ex}} = (1.8 \pm 0.3) \times 10^{-17}$ cm^2, as reported in the main text. Using the two depletion saturation powers obtained for SiV 4 & 5 shown in Figure 3.2c (we omitted SiV 6 because that data

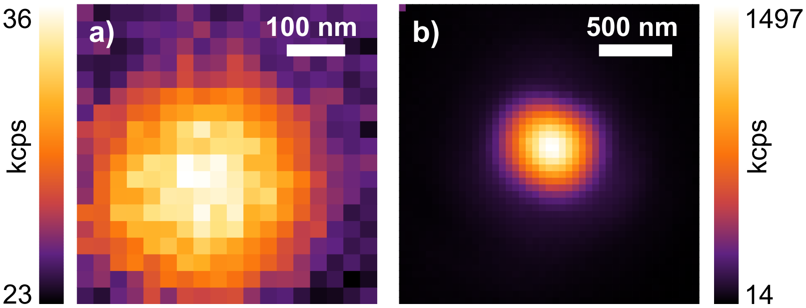

Figure 4.1: **Excitation and depletion beam profiles.** (a) Scanning confocal image of ZPL emission (733–747 nm) from an isolated SiV center excited by 680–700 nm light at 1 mW average power. (b) Scanning confocal image of ZPL emission from an individual bead excited by the Gaussian depletion beam (765–800 nm) at 20 μW average power. The pinhole in the emission path was removed during the scans in both (a) and (b) to make an accurate measurement of the beam profile.

was obtained without measuring the depletion beam's profile using beads immediately beforehand), two values of the stimulated emission cross section (σ_{STED}) were calculated [Eq. (4.4)] and we reported their mean value and standard deviation in the text as $\sigma_{\mathrm{STED}} = (4.0 \pm 0.3) \times 10^{-17}$ cm^2.

4.4 Temporal characterization of laser pulses

The temporal properties of the excitation and depletion pulses were determined by monitoring the fluorescence of SiV centers as a function of the delay between excitation and depletion pulses, Δt. The normalized fluorescence intensity of an isolated SiV center excited ($P_{ex} = 1.5\,\mathrm{mW}$) and depleted ($P_d = 5.0\,\mathrm{mW}$) by Gaussian-spatial-profile pulses were obtained as a function of Δt, shown as red circles in Fig. 4.2b.

To describe the dynamics and extract pulse parameters, we model the SiV center as a closed two-level system under non-resonant optical pumping, Fig. 4.2a. The excitation and depletion pulses are assumed to have a Gaussian temporal profile.

For simplicity, we assume that the FWHM of the temporal profile, τ_p, is the same for both excitation and depletion pulses. Under these assumptions, the time-dependent excited state population of the SiV center, $n_1(t)$, is given by:

$$\frac{d\,n_1(t)}{dt} = \Gamma_{\rm ex}\,{\rm e}^{-4\ln 2\,(\frac{t}{\tau_p})^2}[1-n_1(t)] - [\Gamma_{\rm d}\,{\rm e}^{-4\ln 2\,(\frac{t-\Delta t}{\tau_p})^2} + \frac{1}{\tau_{fl}}]\,n_1(t), \tag{4.5}$$

where Δt is the time-delay between the excitation and depletion beams, $T_{\rm rep} = 12.7$ ns is the pulse sequence repetition period, and $\tau_{fl} = 1.2\,$ns is the SiV excited state lifetime. The excitation and stimulated emission rates are defined as $\Gamma_{\rm ex} = F_{\rm ex}/(\tau_p\,F_{\rm ex,\,sat})$ and $\Gamma_{\rm d} = F_{\rm d}/(\tau_p\,F_{\rm d,\,sat})$, respectively. Based on independent measurements of the excitation and depletion powers and pulse shapes used in experiment, we set $F_{\rm ex}/F_{\rm ex,\,sat} = 1.25$ and $F_{\rm d}/F_{\rm d,\,sat} = 2.0$.

To model the fluorescence intensity, solutions to Eq. (4.5) are obtained numerically and the excited-state population is integrated from $t = 0$ to $t = T_{\rm rep}$.

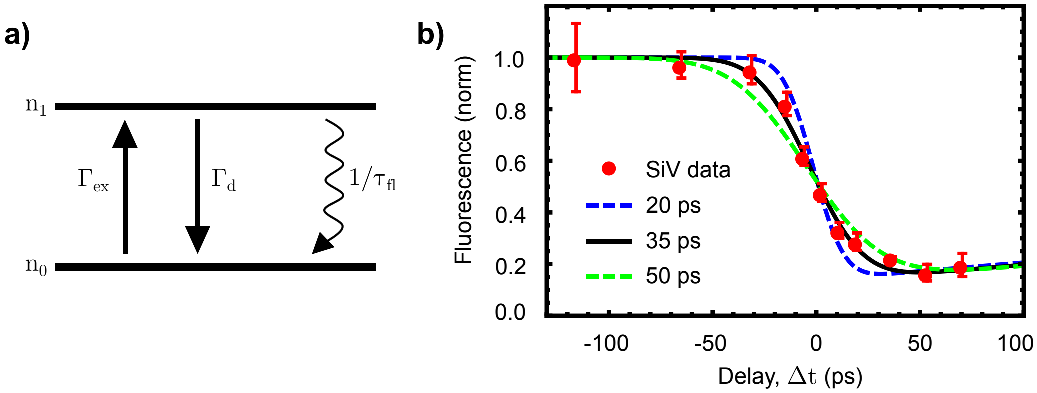

Figure 4.2: **Depletion efficiency Vs time-delay.** (a) Energy levels of a closed two-level atom. $\Gamma_{\rm ex}$, $\Gamma_{\rm d}$ and $1/\tau_{fl}$ are the excitation, stimulated emission and spontaneous emission rates, respectively. (b) Red circles: normalized fluorescence intensity of an isolated SiV center excited at $P_{ex} = 1.5\,$mW and depleted at $P_d = 5.0\,$mW for different time delays between the excitation and depletion beams. For each delay, three measurements were taken and the data points and error bars are their mean and standard deviation, respectively. Theoretical curves based on Eq. (4.5) are plotted for three FWHM pulse widths, $\tau_p = 20,\ 35,$ and 50 ps.

We assume that at the beginning of each sequence the SiV center is in the ground state, $n_1(0) = 0$. In Fig. 4.2b, the normalized integrated excited-state population is plotted as a function of time delay (Δt) for three different values of pulse width (τ_p). The FWHM pulse length that best matches the experimental data is $\tau_p = 35$ ps.

It can be seen from Fig. 4.2b that the depletion efficiency is maximized when $\Delta t \approx \tau_p$. For all experiments reported in the main text, we set the time delay between pulses by maximizing the depletion efficiency. We therefore assume the time delay was in the range 35 ps $\lesssim \Delta t \lesssim$ 100 ps.

4.5 Lateral PSF in STED microscopy

The donut quality of the STED beam plays a major role in achieving high resolution in STED microscopy. To measure the experimental donut profile, we recorded a

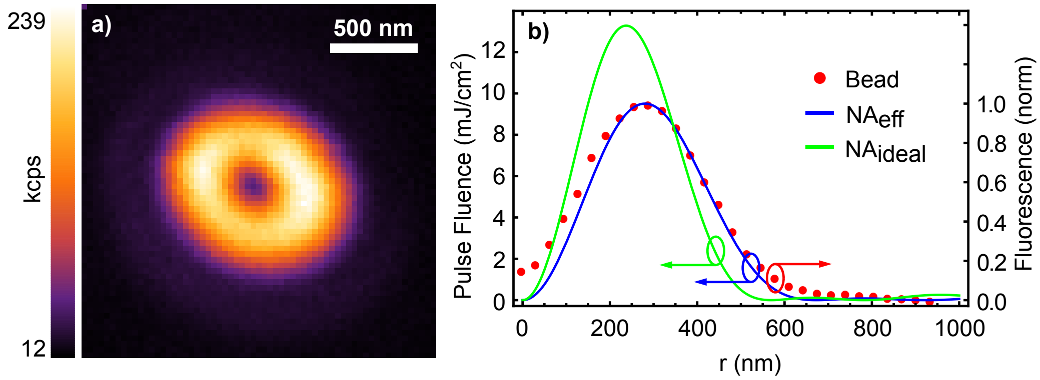

Figure 4.3: **Donut quality.** (a) Scanning confocal image (with pinhole removed) of ZPL emission from an individual bead excited by the donut beam (765–800 nm). (b) Left axis: theoretical pulse fluence profile of a donut-shaped beam, Eq. (4.6), as a function of radial distance. The profile is plotted for $P_{\text{donut}} = 4.75\,\text{mW}$ and $\lambda = 790\,\text{nm}$ with $\text{NA}_{\text{eff}} = 1.1$ (blue) and $\text{NA}_{\text{ideal}} = 1.3$ (green). Right axis: the normalized fluorescence intensity profile of the bead image in (a) determined from the average of four line-cuts beginning at the donut's center.

scanning confocal (but with pinhole removed) anti-Stokes fluorescent image of an individual bead excited by our donut-shaped STED beam, Figure 4.3a. An average of four line-cuts beginning at the donut' s center is shown as red circles in Fig. 4.3b.

To compare to the theoretical optimal donut profile, we assume that the vortex phase plate converts a coherent plane wave into an ideal Laguerre-Gaussian donut beam. The donut pulse fluence profile in the focal plane of the objective lens, $F_{\text{donut}}(r)$, can then be approximated as [96]:

$$F_{\text{donut}}(r) = P_{\text{donut}}\, T_{\text{rep}} \frac{\pi \text{NA}^2}{\lambda^2} \left(\pi \frac{H_0(u)J_1(u) - H_1(u)J_0(u)}{u} \right)^2 . \qquad (4.6)$$

Here P_{donut} is the average donut power, $T_{\text{rep}} = 12.7$ ns is the pulse repetition period, $u = 2\pi r \text{NA}/\lambda$ is the normalized radial distance, λ is the wavelength of the donut beam, NA is the objective numerical aperture, J_0 and J_1 are the zeroth and first order Bessel Functions, and H_0 and H_1 are the zeroth and first order Struve Functions.

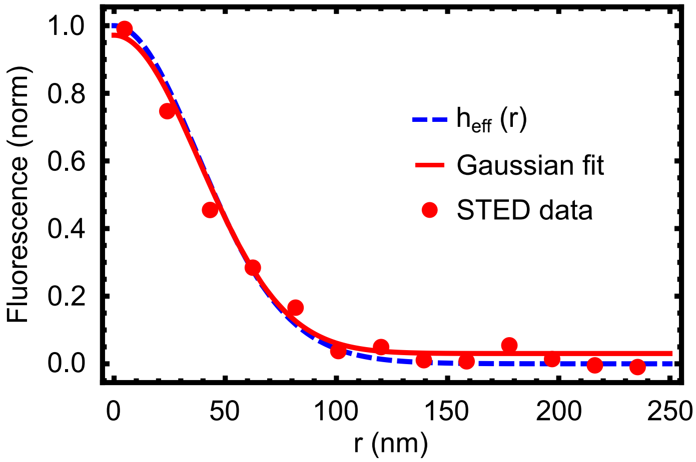

Figure 4.4: **The effective PSF in STED microscopy.** Red circles: normalized STED fluorescence intensity profile of SiV 7 using $P_{\text{donut}} = 32\,\text{mW}$ (Fig. 3.3d). Solid red line: a Gaussian fit to the data revealing a FWHM $\Delta d \approx 90$ nm. Dashed blue line: theoretical STED PSF, $h_{eff}(r)$, determined from Eqs. (4.6) and (4.7). The parameters used in the calculation are: $D = 270\,\text{nm}$, $P_{\text{donut}} = 32\,\text{mW}$, $\lambda = 790\,\text{nm}$, $\text{NA}_{\text{eff}} = 1.1$ and $F_{\text{d, sat}} = 6.8\ \text{mJ/cm}^2$.

Figure 4.3b shows plots of $F_{\text{donut}}(r)$, calculated from Eq. (4.6), for two values of NA. The two values correspond to the true objective numerical aperture, $\text{NA}_{\text{ideal}} = 1.3$, and an effective numerical aperture, $\text{NA}_{\text{eff}} = 1.1$, that best fits the experimental profile. The difference between the optimal donut profile ($\text{NA}_{\text{ideal}} = 1.3$) and the experimental profile ($\text{NA}_{\text{eff}} = 1.1$) may be due to a combination of imperfect circular polarization, deviations from the plane wave approximation before the vortex phase plate, and/or under-filling of the beam at the objective's back aperture.

The $\text{NA}_{\text{eff}} = 1.1$ profile was used to convert the average donut power, P_{donut}, into peak donut pulse fluence in Fig. 3.3a. The characteristic saturation powers, $P_{\text{donut, sat}} = 4.7$ and $4.8\,\text{mW}$, obtained for the two isolated SiV centers shown in Fig. 3.3a correspond to peak donut pulse fluences of 9.5 and 9.7 mJ/cm^2, respectively.

To understand the relationship between donut quality and STED resolution, we define the lateral STED point-spread function (PSF) as [87]:

$$h_{eff}(r) = h_c(r)\ \mathrm{e}^{-F_{\text{donut}}(r)/F_{\text{d,sat}}}, \tag{4.7}$$

where $h_c(r) \approx \mathrm{e}^{-4\ln 2\,(r/D)^2}$ is the confocal PSF with a FWHM of $D = 270$ nm. Figure 4.4 plots $h_{eff}(r)$ using $F_{\text{d, sat}} = 6.8$ mJ/cm^2. The pulse fluence, $F_{\text{donut}}(r)$ was computed from Eq. (4.6) using $\text{NA}_{\text{eff}} = 1.1$, $\lambda = 790$ nm, and $P_{\text{donut}} = 32$ mW (the highest power used in our experiments). The theoretical STED PSF is in excellent agreement with the experimental PSF obtained at this power and is well approximated by a circular Gaussian function with FWHM $\Delta d = 90$ nm. For all experiments in the main text we used the circular Gaussian profile approximation to extract the resolution to simplify analysis.

4.6 Fluorescence intensity distribution of isolated SiV centers

In order to determine whether the isolated SiV centers in our samples are really single emitters or not, we recorded large fluorescent images ($10 \times 10\,\mu\text{m}^2$) of the dense sample in both confocal and STED configurations. The distribution of the peak SiV fluorescence intensities in both cases is shown in Fig. 4.5. The narrow distribution suggests that the features likely arise from single emitters with relatively homogenous photophysical properties. However, the main conclusions in this work (STED cross section, resolution, etc.) would remain valid even if these isolated fluorescent features came from multiple emitters.

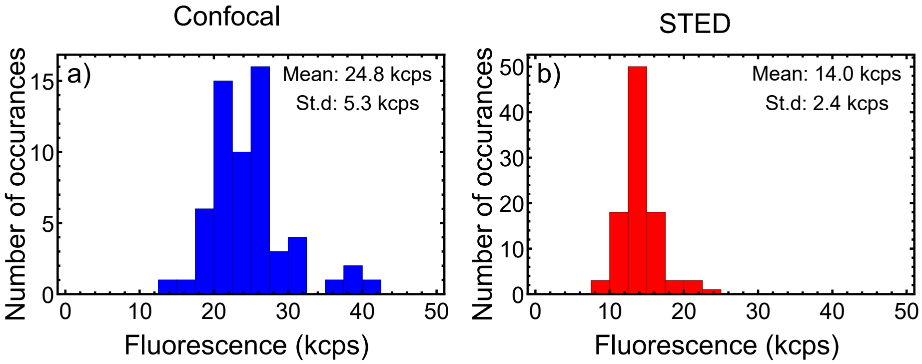

Figure 4.5: **Fluorescence intensity distribution of isolated SiV centers.** Distribution of fluorescence intensity of isolated SiV centers in (a) confocal and (b) STED images. Data were obtained from the same region on the high-density sample (SiV density: $\sim 10^8$ cm^{-2}) within an area of 10×10 μm^2 at $P_{ex} = 2.1$ mW and $P_{\text{donut}} = 32$ mW. The insets in (a) and (b) are the mean number and standard deviation of the corresponding distributions.

4.7 Anti-Stokes excitation

As discussed in the main text, a faint halo background can sometimes be observed in STED images of isolated SiV centers. This background follows closely the STED donut profile and likely arises from anti-Stokes emission. At room temperature, the SiV center has a small (but non-zero) probability of being in an excited vibrational level within the ground-state manifold [97]. Thus the STED beam has a small probability to excite SiV centers in addition to its primary role of stimulating emission from the excited state. For high STED intensities, this anti-Stokes excitation phenomenon can reduce the contrast of STED images and limit the achievable resolution [98, 99]. Thus, for STED microscopy with fluorophores having a relatively small Stokes shift, as is the case for SiV centers (Fig. 3.1b), there is a trade off between increasing σ_{STED} (by exciting at the peak of the phonon sideband) and introducing background due to anti-Stokes excitation.

Figure 4.6a shows a STED image of an isolated SiV center taken at the highest available donut power in our setup, ($P_{\text{donut}} = 35.2\,\text{mW}$). A weak halo of background

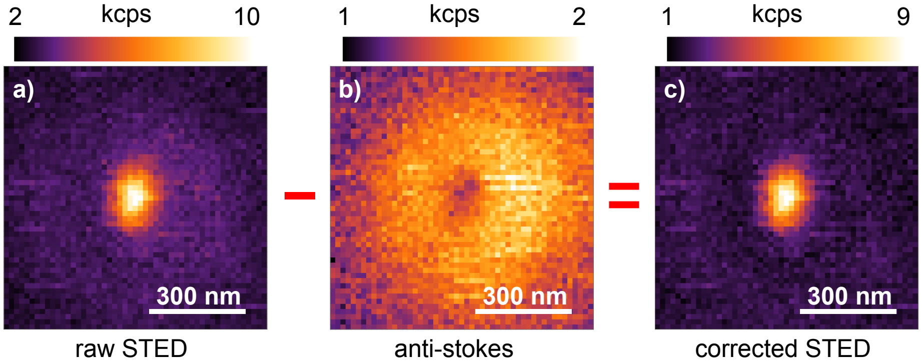

Figure 4.6: **Anti-Stokes excitation of a SiV center.** (a) Raw STED image of an isolated SiV center taken at $P_{\text{ex}} = 1.1$ mW and $P_{\text{donut}} = 35.2$ mW. (b) Weighted anti-Stokes fluorescent image of the same SiV center taken at $P_{\text{ex}} = 0$ mW and $P_{\text{donut}} = 35.2$ mW. (c) The corrected STED image after subtracting the anti-Stokes background fluorescence.

fluorescence is observed. By blocking the excitation beam and recording another image, Fig. 4.6b, it is seen that this weak background ($\sim$ 1 kcps) follows the shape of the donut profile. This background image can be subtracted from the raw STED images in order to improve the image contrast, Fig. 4.6c.

References

[1] Gordon Davies and M. F. Hamer. Optical studies of the 1.945 eV vibronic band in diamond. *Proceedings of the Royal Society of London. A. Mathematical and Physical Sciences*, 348(1653):285–298, feb 1976.

[2] J H N Loubser and J A van Wyk. Electron spin resonance in the study of diamond. *Reports on Progress in Physics*, 41(8):1201–1248, aug 1978.

[3] A. Gruber. Scanning Confocal Optical Microscopy and Magnetic Resonance on Single Defect Centers. *Science*, 276(5321):2012–2014, jun 1997.

[4] Charles Santori, Philippe Tamarat, Philipp Neumann, Jörg Wrachtrup, David Fattal, Raymond G. Beausoleil, James Rabeau, Paolo Olivero, Andrew D. Greentree, Steven Prawer, Fedor Jelezko, and Philip Hemmer. Coherent Population Trapping of Single Spins in Diamond under Optical Excitation. *Physical Review Letters*, 97(24):247401, dec 2006.

[5] Ph Tamarat, T. Gaebel, J. R. Rabeau, M. Khan, A. D. Greentree, H. Wilson, L. C. L. Hollenberg, S. Prawer, P. Hemmer, F. Jelezko, and J. Wrachtrup. Stark Shift Control of Single Optical Centers in Diamond. *Physical Review Letters*, 97(8):083002, aug 2006.

[6] Ph Tamarat, N. B. Manson, J. P. Harrison, R. L. McMurtrie, A. Nizovtsev, C. Santori, R. G. Beausoleil, P. Neumann, T. Gaebel, F. Jelezko, P. Hemmer, and J. Wrachtrup. Spin-flip and spin-conserving optical transitions of the nitrogen-vacancy centre in diamond. *New Journal of Physics*, 10(4):045004, apr 2008.

[7] V. M. Acosta, E. Bauch, M. P. Ledbetter, C. Santori, K.-M. C. Fu, P. E. Barclay, R. G. Beausoleil, H. Linget, J. F. Roch, F. Treussart, S. Chemerisov, W. Gawlik, and D. Budker. Diamonds with a high density of nitrogen-vacancy centers for magnetometry applications. *Physical Review B*, 80(11):115202, sep 2009.

[8] V. M. Acosta, E. Bauch, M. P. Ledbetter, A. Waxman, L.-S. Bouchard, and D. Budker. Temperature Dependence of the Nitrogen-Vacancy Magnetic Resonance in Diamond. *Physical Review Letters*, 104(7):070801, feb 2010.

[9] F. Dolde, I. Jakobi, B. Naydenov, N. Zhao, S. Pezzagna, C. Trautmann, J. Meijer, P. Neumann, F. Jelezko, and J. Wrachtrup. Room-temperature entanglement between single defect spins in diamond. *Nature Physics*, 9(3):139–143, mar 2013.

[10] B. Hensen, H. Bernien, A. E. Dréau, A. Reiserer, N. Kalb, M. S. Blok, J. Ruitenberg, R. F. L. Vermeulen, R. N. Schouten, C. Abellán, W. Amaya, V. Pruneri, M. W. Mitchell, M. Markham, D. J. Twitchen, D. Elkouss, S. Wehner, T. H. Taminiau, and R. Hanson. Loophole-free Bell inequality violation using electron spins separated by 1.3 kilometres. *Nature*, 526(7575):682–686, oct 2015.

[11] Janis Smits, Joshua T. Damron, Pauli Kehayias, Andrew F. McDowell, Nazanin Mosavian, Ilja Fescenko, Nathaniel Ristoff, Abdelghani Laraoui, Andrey Jarmola, and Victor M. Acosta. Two-dimensional nuclear magnetic resonance spectroscopy with a microfluidic diamond quantum sensor. *Science Advances*, 5(7):eaaw7895, jul 2019.

[12] Shu-Jung Yu, Ming-Wei Kang, Huan-Cheng Chang, Kuan-Ming Chen, and Yueh-Chung Yu. Bright Fluorescent Nanodiamonds: No Photobleaching and Low Cytotoxicity. *Journal of the American Chemical Society*, 127(50):17604–17605, dec 2005.

[13] Chi-Cheng Fu, Hsu-Yang Lee, Kowa Chen, Tsong-Shin Lim, Hsiao-Yun Wu, Po-Keng Lin, Pei-Kuen Wei, Pei-Hsi Tsao, Huan-Cheng Chang, and Wunshain Fann. Characterization and application of single fluorescent nanodiamonds as cellular biomarkers. *Proceedings of the National Academy of Sciences*, 104(3):727–732, jan 2007.

[14] V. Vaijayanthimala and H-C Chang. Functionalized fluorescent nanodiamonds for biomedical applications. *Nanomedicine*, 4(1):47–55, jan 2009.

[15] Nitin Mohan, Chao-Sheng Chen, Hsiao-Han Hsieh, Yi-Chun Wu, and Huan-Cheng Chang. In Vivo Imaging and Toxicity Assessments of Fluorescent Nanodiamonds in Caenorhabditis elegans. *Nano Letters*, 10(9):3692–3699, sep 2010.

[16] Yan-Kai Tzeng, Orestis Faklaris, Be-Ming Chang, Yung Kuo, Jui-Hung Hsu, and Huan-Cheng Chang. Superresolution Imaging of Albumin-Conjugated Fluorescent Nanodiamonds in Cells by Stimulated Emission Depletion. *Angewandte Chemie International Edition*, 50(10):2262–2265, mar 2011.

[17] G. Kucsko, P. C. Maurer, N. Y. Yao, M. Kubo, H. J. Noh, P. K. Lo, H. Park, and M. D. Lukin. Nanometre-scale thermometry in a living cell. *Nature*, 500(7460):54–58, aug 2013.

[18] C. Bradac, T. Gaebel, N. Naidoo, M. J. Sellars, J. Twamley, L. J. Brown, A. S. Barnard, T. Plakhotnik, A. V. Zvyagin, and J. R. Rabeau. Observation and control of blinking nitrogen-vacancy centres in discrete nanodiamonds. *Nature Nanotechnology*, 5(5):345–349, may 2010.

[19] Min Gu, Yaoyu Cao, Stefania Castelletto, Betty Kouskousis, and Xiangping Li. Super-resolving single nitrogen vacancy centers within single nanodiamonds using a localization microscope. *Optics Express*, 21(15):17639, jul 2013.

[20] Igor I. Vlasov, Andrey A. Shiryaev, Torsten Rendler, Steffen Steinert, Sang-Yun Lee, Denis Antonov, Márton Vörös, Fedor Jelezko, Anatolii V. Fisenko, Lubov F. Semjonova, Johannes Biskupek, Ute Kaiser, Oleg I. Lebedev, Ilmo Sildos, Philip R. Hemmer, Vitaly I. Konov, Adam Gali, and Jörg Wrachtrup. Molecular-sized fluorescent nanodiamonds. *Nature Nanotechnology*, 9(1):54–58, jan 2014.

[21] Lijin Xia, Scott Lenaghan, and Mingjun Zhang. Naturally Occuring Nanofiber Network from the Sundew for Tissue Engineering. 2015.

[22] 8x57is / CC BY-SA 4.0. Multicolor fluorescence image of living HeLa cells, 2014.

[23] Fabian Göttfert, Christian A. Wurm, Veronika Mueller, Sebastian Berning, Volker C. Cordes, Alf Honigmann, and Stefan W. Hell. Coaligned Dual-Channel STED Nanoscopy and Molecular Diffusion Analysis at 20 nm Resolution. *Biophysical Journal*, 105(1):L01–L03, jul 2013.

[24] Matthew D. Lew, Steven F. Lee, Michael A. Thompson, Hsiao-lu D. Lee, and W. E. Moerner. Single-Molecule Photocontrol and Nanoscopy. In *Far-Field Optical Nanoscopy*, chapter 4, pages 87–110. Springer, 2012.

[25] Eric Betzig, George H. Patterson, Rachid Sougrat, O. Wolf Lindwasser, Scott Olenych, Juan S. Bonifacino, Michael W. Davidson, Jennifer Lippincott-Schwartz, and Harald F. Hess. Imaging Intracellular Fluorescent Proteins at Nanometer Resolution. *Science*, 313(5793):1642–1645, sep 2006.

[26] Samuel T. Hess, Thanu P.K. Girirajan, and Michael D. Mason. Ultra-High Resolution Imaging by Fluorescence Photoactivation Localization Microscopy. *Biophysical Journal*, 91(11):4258–4272, dec 2006.

[27] Michael J. Rust, Mark Bates, and Xiaowei Zhuang. Sub-diffraction-limit imaging by stochastic optical reconstruction microscopy (STORM). *Nature Methods*, 3(10):793–796, oct 2006.

[28] Stefan W. Hell and Jan Wichmann. Breaking the diffraction resolution limit by stimulated emission: stimulated-emission-depletion fluorescence microscopy. *Optics Letters*, 19(11):780, jun 1994.

[29] S. W. Hell and M. Kroug. Ground-state-depletion fluorscence microscopy: A concept for breaking the diffraction resolution limit. *Applied Physics B Lasers and Optics*, 60(5):495–497, may 1995.

[30] Chunlang Wang, Christian Kurtsiefer, Harald Weinfurter, and Bernd Burchard. Single photon emission from SiV centres in diamond produced by ion implantation. *Journal of Physics B: Atomic, Molecular and Optical Physics*, 39(1):37–41, jan 2006.

[31] Jean-Claude M. Diels, Joel J. Fontaine, Ian C. McMichael, and Francesco Simoni. Control and measurement of ultrashort pulse shapes (in amplitude and phase) with femtosecond accuracy. *Applied Optics*, 24(9):1270, may 1985.

[32] J.W. Goodman. Introduction to Fourier Optics 3ed, 2005.

[33] M Born and E Wolf. *Principles of optics: electromagnetic theory of propagation, interference ...* Cambridge University Press, 1999.

[34] E Hecht. *Optics*. Pearson, 5th edition, 2016.

[35] Jonathan Leach, Eric Yao, and Miles J. Padgett. Observation of the vortex structure of a non-integer vortex beam. *New Journal of Physics*, 6:71–71, jul 2004.

[36] Bhanu Neupane, Fang Chen, Wei Sun, Daniel T. Chiu, and Gufeng Wang. Tuning donut profile for spatial resolution in stimulated emission depletion microscopy. *Review of Scientific Instruments*, 84(4):043701, apr 2013.

[37] Djenan Ganic, Xiaosong Gan, and Min Gu. Focusing of doughnut laser beams by a high numerical-aperture objective in free space. *Optics Express*, 11(21):2747, oct 2003.

[38] K. Bahlmann and S. W. Hell. Electric field depolarization in high aperture focusing with emphasis on annular apertures. *Journal of Microscopy*, 200(1):59–67, oct 2000.

[39] Xiang Hao, Cuifang Kuang, Tingting Wang, and Xu Liu. Effects of polarization on the de-excitation dark focal spot in STED microscopy. *Journal of Optics*, 12(11):115707, nov 2010.

[40] J. F. Ziegler, J. P. Biersack, and M. D. Ziegler. *SRIM - The Stopping and Range of Ions in Matter*. James Ziegler, 2015.

[41] Materialscientist / CC BY-SA 3.0. NVple, 2008.

[42] Marcus W. Doherty, Neil B. Manson, Paul Delaney, Fedor Jelezko, Jörg Wrachtrup, and Lloyd C.L. Hollenberg. The nitrogen-vacancy colour centre in diamond. *Physics Reports*, 528(1):1–45, jul 2013.

[43] Arthur N. Newell, Dontray A. Dowdell, and D. H. Santamore. Surface effects on nitrogen vacancy centers neutralization in diamond. *Journal of Applied Physics*, 120(18):185104, nov 2016.

[44] K. Ohashi, T. Rosskopf, H. Watanabe, M. Loretz, Y. Tao, R. Hauert, S. Tomizawa, T. Ishikawa, J. Ishi-Hayase, S. Shikata, C. L. Degen, and K. M. Itoh. Negatively Charged Nitrogen-Vacancy Centers in a 5 nm Thin 12 C Diamond Film. *Nano Letters*, 13(10):4733–4738, oct 2013.

[45] Carlo Bradac, Torsten Gaebel, Chris I. Pakes, Jana M. Say, Andrei V. Zvyagin, and James R. Rabeau. Effect of the Nanodiamond Host on a Nitrogen-Vacancy Color-Centre Emission State. *Small*, 9(1):132–139, jan 2013.

[46] K.-M. C. Fu, C. Santori, P. E. Barclay, and R. G. Beausoleil. Conversion of neutral nitrogen-vacancy centers to negatively charged nitrogen-vacancy centers through selective oxidation. *Applied Physics Letters*, 96(12):121907, mar 2010.

[47] M. V. Hauf, B. Grotz, B. Naydenov, M. Dankerl, S. Pezzagna, J. Meijer, F. Jelezko, J. Wrachtrup, M. Stutzmann, F. Reinhard, and J. A. Garrido. Chemical control of the charge state of nitrogen-vacancy centers in diamond. *Physical Review B*, 83(8):081304, feb 2011.

[48] Vladimíra Petráková, Miloš Nesládek, Andrew Taylor, František Fendrych, Petr Cígler, Miroslav Ledvina, Jiří Vacík, Jan Štursa, and Jan Kučka. Luminescence properties of engineered nitrogen vacancy centers in a close surface proximity. *physica status solidi (a)*, 208(9):2051–2056, sep 2011.

[49] Bernhard Grotz, Moritz V. Hauf, Markus Dankerl, Boris Naydenov, Sébastien Pezzagna, Jan Meijer, Fedor Jelezko, Jörg Wrachtrup, Martin Stutzmann, Friedemann Reinhard, and Jose A. Garrido. Charge state manipulation of qubits in diamond. *Nature Communications*, 3(1):729, jan 2012.

[50] Peter Deák, Bálint Aradi, Moloud Kaviani, Thomas Frauenheim, and Adam Gali. Formation of NV centers in diamond: A theoretical study based on calculated transitions and migration of nitrogen and vacancy related defects. *Physical Review B*, 89(7):075203, feb 2014.

[51] T. Goulet, A. Bernas, C. Ferradini, and J.-P. Jay-Gerin. On the electronic structure of liquid water: Conduction-band tail revealed by photoionization data. *Chemical Physics Letters*, 170(5-6):492–496, jul 1990.

[52] Giorgia Olivieri, Alok Goel, Armin Kleibert, Dean Cvetko, and Matthew A. Brown. Quantitative ionization energies and work functions of aqueous solutions. *Physical Chemistry Chemical Physics*, 18(42):29506–29515, 2016.

[53] Zhen Zhang and John T. Yates. Band Bending in Semiconductors: Chemical and Physical Consequences at Surfaces and Interfaces. *Chemical Reviews*, 112(10):5520–5551, oct 2012.

[54] Charles Kittel. *Introduction to Solid State Physics, 8th edition.* Wiley & Sons, New York, NY, 8th edition, 2004.

[55] F. Maier, J. Ristein, and L. Ley. Electron affinity of plasma-hydrogenated and chemically oxidized diamond (100) surfaces. *Physical Review B*, 64(16):165411, oct 2001.

[56] Yaser Silani, Forrest Hubert, and Victor M. Acosta. Stimulated Emission Depletion Microscopy with Diamond Silicon Vacancy Centers. *ACS Photonics*, 6(10):2577–2582, oct 2019.

[57] Thomas A. Klar and Stefan W. Hell. Subdiffraction resolution in far-field fluorescence microscopy. *Optics Letters*, 24(14):954, jul 1999.

[58] Volker Westphal and Stefan W. Hell. Nanoscale Resolution in the Focal Plane of an Optical Microscope. *Physical Review Letters*, 94(14):143903, apr 2005.

[59] Stefan W. Hell. Toward fluorescence nanoscopy. *Nature Biotechnology*, 21(11):1347–1355, nov 2003.

[60] James Pawley. *Handbook Of Biological Confocal Microscopy.* Springer US, Boston, MA, third edition, 2006.

[61] Christian A. Wurm, Kirill Kolmakov, Fabian Göttfert, Haisen Ta, Mariano Bossi, Heiko Schill, Sebastian Berning, Stefan Jakobs, Gerald Donnert, Vladimir N. Belov, and Stefan W. Hell. Novel red fluorophores with superior performance in STED microscopy. *Optical Nanoscopy*, 1(1):7, 2012.

[62] M. Sameiro T. Gonçalves. Fluorescent Labeling of Biomolecules with Organic Probes. *Chemical Reviews*, 109(1):190–212, jan 2009.

[63] Raphael Alford, Haley M. Simpson, Josh Duberman, G. Craig Hill, Mikako Ogawa, Celeste Regino, Hisataka Kobayashi, and Peter L. Choyke. Toxicity of Organic Fluorophores Used in Molecular Imaging: Literature Review. *Molecular Imaging*, 8(6):7290.2009.00031, nov 2009.

[64] Graham T. Dempsey, Joshua C. Vaughan, Kok Hao Chen, Mark Bates, and Xiaowei Zhuang. Evaluation of fluorophores for optimal performance in localization-based super-resolution imaging. *Nature Methods*, 8(12):1027–1036, dec 2011.

[65] Margaux Bouzin, Giuseppe Chirico, Laura D'Alfonso, Laura Sironi, Giancarlo Soavi, Giulio Cerullo, Barbara Campanini, and Maddalena Collini. Stimulated Emission Properties of Fluorophores by CW-STED Single Molecule Spectroscopy. *The Journal of Physical Chemistry B*, 117(51):16405–16415, dec 2013.

[66] G. Donnert, J. Keller, R. Medda, M. A. Andrei, S. O. Rizzoli, R. Luhrmann, R. Jahn, C. Eggeling, and S. W. Hell. Macromolecular-scale resolution in biological fluorescence microscopy. *Proceedings of the National Academy of Sciences*, 103(31):11440–11445, aug 2006.

[67] C. Eggeling, J. Widengren, R. Rigler, and C. A. M. Seidel. Photobleaching of Fluorescent Dyes under Conditions Used for Single-Molecule Detection: Evidence of Two-Step Photolysis. *Analytical Chemistry*, 70(13):2651, jul 1998.

[68] Joanna Oracz, Volker Westphal, Czesław Radzewicz, Steffen J. Sahl, and Stefan W. Hell. Photobleaching in STED nanoscopy and its dependence on the photon flux applied for reversible silencing of the fluorophore. *Scientific Reports*, 7(1):11354, dec 2017.

[69] Igor Aharonovich and Elke Neu. Diamond nanophotonics. *Advanced Optical Materials*, 2(10):911–928, 2014.

[70] Julia Tisler, Gopalakrishnan Balasubramanian, Boris Naydenov, Roman Kolesov, Bernhard Grotz, Rolf Reuter, Jean Paul Boudou, Patrick A. Curmi, Mohamed Sennour, Alain Thorel, Michael Börsch, Kurt Aulenbacher, Rainer Erdmann, Philip R. Hemmer, Fedor Jelezko, and Jörg Wrachtrup. Fluorescence and spin properties of defects in single digit nanodiamonds. *ACS Nano*, 3(7):1959–1965, 2009.

[71] Han B. Man and Dean Ho. Nanodiamonds as Platforms for Biology and Medicine. *Journal of Laboratory Automation*, 18(1):12–18, feb 2013.

[72] Dominik Wildanger, Brian R. Patton, Heiko Schill, Luca Marseglia, J. P. Hadden, Sebastian Knauer, Andreas Schönle, John G. Rarity, Jeremy L. O'Brien, Stefan W. Hell, and Jason M. Smith. Solid Immersion Facilitates Fluorescence Microscopy with Nanometer Resolution and Sub-Ångström Emitter Localization. *Advanced Materials*, 24(44):OP309–OP313, nov 2012.

[73] Orestis Faklaris, Jacques Botsoa, Thierry Sauvage, Jean-François Roch, and François Treussart. Photoluminescent nanodiamonds: Comparison of the photoluminescence saturation properties of the NV color center and a cyanine dye at the single emitter level, and study of the color center concentration under different preparation conditions. *Diamond and Related Materials*, 19(7-9):988–995, jul 2010.

[74] Kyu Young Han, Katrin I. Willig, Eva Rittweger, Fedor Jelezko, Christian Eggeling, and Stefan W. Hell. Three-Dimensional Stimulated Emission Depletion Microscopy of Nitrogen-Vacancy Centers in Diamond Using Continuous-Wave Light. *Nano Letters*, 9(9):3323–3329, sep 2009.

[75] Eva Rittweger, Kyu Young Han, Scott E. Irvine, Christian Eggeling, and Stefan W. Hell. STED microscopy reveals crystal colour centres with nanometric resolution. *Nature Photonics*, 3(3):144–147, mar 2009.

[76] N. Aslam, G. Waldherr, P. Neumann, F. Jelezko, and J. Wrachtrup. Photo-induced ionization dynamics of the nitrogen vacancy defect in diamond investigated by single-shot charge state detection. *New Journal of Physics*, 15(1):013064, jan 2013.

[77] Luke Hacquebard and Lilian Childress. Charge-state dynamics during excitation and depletion of the nitrogen-vacancy center in diamond. *Physical Review A*, 97(6):063408, jun 2018.

[78] J. R. Rabeau, A. Stacey, A. Rabeau, S. Prawer, F. Jelezko, I. Mirza, and J. Wrachtrup. Single Nitrogen Vacancy Centers in Chemical Vapor Deposited Diamond Nanocrystals. *Nano Letters*, 7(11):3433–3437, nov 2007.

[79] Christian Hepp, Tina Müller, Victor Waselowski, Jonas N. Becker, Benjamin Pingault, Hadwig Sternschulte, Doris Steinmüller-Nethl, Adam Gali, Jeronimo R. Maze, Mete Atatüre, and Christoph Becher. Electronic Structure of the Silicon Vacancy Color Center in Diamond. *Physical Review Letters*, 112(3):036405, jan 2014.

[80] Lachlan J. Rogers, Kay D. Jahnke, Marcus W. Doherty, Andreas Dietrich, Liam P. McGuinness, Christoph Müller, Tokuyuki Teraji, Hitoshi Sumiya, Junichi Isoya, Neil B. Manson, and Fedor Jelezko. Electronic structure of the

negatively charged silicon-vacancy center in diamond. *Physical Review B*, 89(23):235101, jun 2014.

[81] Lars Kastrup and Stefan W. Hell. Absolute optical cross section of individual fluorescent molecules. *Angewandte Chemie - International Edition*, 43(48):6646, 2004.

[82] E. Rittweger, B.R. Rankin, V. Westphal, and S.W. Hell. Fluorescence depletion mechanisms in super-resolving STED microscopy. *Chemical Physics Letters*, 442(4-6):483–487, jul 2007.

[83] Syuto Tamura, Godai Koike, Akira Komatsubara, Tokuyuki Teraji, Shinobu Onoda, Liam P. McGuinness, Lachlan Rogers, Boris Naydenov, E. Wu, Liu Yan, Fedor Jelezko, Takeshi Ohshima, Junichi Isoya, Takahiro Shinada, and Takashi Tanii. Array of bright silicon-vacancy centers in diamond fabricated by low-energy focused ion beam implantation. *Applied Physics Express*, 7(11):115201, nov 2014.

[84] Tim Schröder, Matthew E. Trusheim, Michael Walsh, Luozhou Li, Jiabao Zheng, Marco Schukraft, Alp Sipahigil, Ruffin E. Evans, Denis D. Sukachev, Christian T. Nguyen, Jose L. Pacheco, Ryan M. Camacho, Edward S. Bielejec, Mikhail D. Lukin, and Dirk Englund. Scalable focused ion beam creation of nearly lifetime-limited single quantum emitters in diamond nanostructures. *Nature Communications*, 8(1):15376, aug 2017.

[85] Ingo Gregor, Digambara Patra, and Jörg Enderlein. Optical Saturation in Fluorescence Correlation Spectroscopy under Continuous-Wave and Pulsed Excitation. *ChemPhysChem*, 6(1):164–170, jan 2005.

[86] D Wildanger, R Medda, L Kastrup, and S W Hell. A compact STED microscope providing 3D nanoscale resolution. *Journal of microscopy*, 236(1):35–43, 2009.

[87] B Harke, J Keller, C K Ullal, V Westphal, A Schoenle, and S W Hell. Resolution scaling in STED microscopy. *Optics Express*, 16(6):4154–4162, 2008.

[88] Dominik Wildanger, Eva Rittweger, Lars Kastrup, and Stefan W Hell. STED microscopy with a supercontinuum laser source. *Optics express*, 16(13):9614–21, 2008.

[89] M. J. Crane, A. Petrone, R. A. Beck, M. B. Lim, X. Zhou, X. Li, R. M. Stroud, and P. J. Pauzauskie. High-pressure, high-temperature molecular doping of nanodiamond. *Science Advances*, 5(5):eaau6073, may 2019.

[90] Elke Neu, David Steinmetz, Janine Riedrich-Möller, Stefan Gsell, Martin Fischer, Matthias Schreck, and Christoph Becher. Single photon emission from silicon-vacancy colour centres in chemical vapour deposition nano-diamonds on iridium. *New Journal of Physics*, 13(2):025012, feb 2011.

[91] J. M. Higbie, J. D. Perreault, V. M. Acosta, C. Belthangady, P. Lebel, M. H. Kim, K. Nguyen, V. Demas, V. Bajaj, and C. Santori. Multiphoton-Excited Fluorescence of Silicon-Vacancy Color Centers in Diamond. *Physical Review Applied*, 7(5):054010, may 2017.

[92] Elke Neu, Christian Hepp, Michael Hauschild, Stefan Gsell, Martin Fischer, Hadwig Sternschulte, Doris Steinmüller-Nethl, Matthias Schreck, and Christoph Becher. Low-temperature investigations of single silicon vacancy colour centres in diamond. *New Journal of Physics*, 15(4):043005, apr 2013.

[93] Christian T. Nguyen, Ruffin E. Evans, Alp Sipahigil, Mihir K. Bhaskar, Denis D. Sukachev, Viatcheslav N. Agafonov, Valery A. Davydov, Liudmila F. Kulikova, Fedor Jelezko, and Mikhail D. Lukin. All-optical nanoscale thermometry with silicon-vacancy centers in diamond. *Applied Physics Letters*, 112(20):203102, may 2018.

[94] P. Kehayias, A. Jarmola, N. Mosavian, I. Fescenko, F. M. Benito, A. Laraoui, J. Smits, L. Bougas, D. Budker, A. Neumann, S. R. J. Brueck, and V. M. Acosta. Solution nuclear magnetic resonance spectroscopy on a nanostructured diamond chip. *Nature Communications*, 8(1):188, dec 2017.

[95] Ruffin E. Evans, Alp Sipahigil, Denis D. Sukachev, Alexander S. Zibrov, and Mikhail D. Lukin. Narrow-Linewidth Homogeneous Optical Emitters in Diamond Nanostructures via Silicon Ion Implantation. *Physical Review Applied*, 5(4):044010, apr 2016.

[96] S.N. Khonina, V.V. Kotlyar, M.V. Shinkaryev, V.A. Soifer, and G.V. Uspleniev. The Phase Rotor Filter. *Journal of Modern Optics*, 39(5):1147–1154, may 1992.

[97] Toan Trong Tran, Blake Regan, Evgeny A. Ekimov, Zhao Mu, Yu Zhou, Wei-bo Gao, Prineha Narang, Alexander S. Solntsev, Milos Toth, Igor Aharonovich, and Carlo Bradac. Anti-Stokes excitation of solid-state quantum emitters for nanoscale thermometry. *Science Advances*, 5(5):eaav9180, may 2019.

[98] Stefan W. Hell, Andreas Schönle, and A. Van den Bos. Nanoscale Resolution in Far-Field Fluorescence Microscopy. In *Science of Microscopy*, pages 790–834. Springer New York, New York, NY, 2007.

[99] Giuseppe Vicidomini, Gael Moneron, Christian Eggeling, Eva Rittweger, and Stefan W. Hell. STED with wavelengths closer to the emission maximum. *Optics Express*, 20(5):5225–5236, 2012.